ISTANBUL TECHNICAL UNIVERSITY ★ INFORMATICS INSTITUTE

**3D SCALAR IMAGING OF DIELECTRIC OBJECTS
BURIED UNDER A ROUGH SURFACE**

Ph.D. THESIS

Evrim TETİK

Department of Communication Systems

Satellite Communication and Remote Sensing Programme

NOVEMBER 2015

ISTANBUL TECHNICAL UNIVERSITY ★ INFORMATICS INSTITUTE

3D SCALAR IMAGING OF DIELECTRIC OBJECTS BURIED UNDER A ROUGH SURFACE

Ph.D. THESIS

Evrim TETİK
(705072003)

Department of Communication Systems

Satellite Communication and Remote Sensing Programme

Thesis Advisor: Prof. Dr. Ibrahim AKDUMAN

NOVEMBER 2015

İSTANBUL TEKNİK ÜNİVERSİTESİ ★ BİLİŞİM ENSTİTÜSÜ

ENGEBELİ YÜZEY ALTINA GÖMÜLÜ DİELEKTRİK CİSİMLERİN ÜÇ BOYUTLU SKALER DURUMDA GÖRÜNTÜLENMESİ

DOKTORA TEZİ

Evrim TETİK
(705072003)

İletişim Sistemleri Anabilim Dalı

Uydu Haberleşmesi ve Uzaktan Algılama Programı

Tez Danışmanı: Prof. Dr. İbrahim AKDUMAN

KASIM 2015

Evrim TETİK, a Ph.D. student of ITU Informatics Institute 705072003, successfully defended the thesis entitled "3D SCALAR IMAGING OF DIELECTRIC OBJECTS BURIED UNDER A ROUGH SURFACE", which she prepared after fulfilling the requirements specified in the associated legislations, before the jury whose signatures are below.

Thesis Advisor :   **Prof. Dr. İbrahim AKDUMAN**   ....
İstanbul Technical Universtiy

Jury Members :   **Prof. Dr. Ali YAPAR**   ....
İstanbul Technical University

Prof. Dr. Sedef KENT   ....
İstanbul Technical University

Prof. Dr. Hülya ŞAHİNTÜRK   ....
Yıldız Technical University

Assoc. Prof. Dr. Tanju YELKENCİ   ....
Marmara University

Date of Submission : September 15, 2015
Date of Defence   : November 11, 2015

To my beloved parents, Necibe and Ismet,

FOREWORD

I would like to express my immense gratitude to Prof. Dr. İbrahim AKDUMAN, who gave me the opportunity to do research under his supervision, for his precious guidance and support during this study. I would also like to deeply thank Dr. Onan GUREN for her contribution and support, but above all, my mother Necibe and my father Ismet, for their infinite love, and unconditional support.

September 2015   Evrim TETIK

x

TABLE OF CONTENTS

ABBREVIATIONS

BOA : Buried Object Approach
CSI : Contrast Source Inversion
CG : Conjugate Gradient
MoM : Method of Moments
SNR : Signal to Noise Ratio

SYMBOLS

Γ	: Surface of the rough interface
T	: Surface of point sources
R	: Measurement surface
D	: Reconstruction domain
C	: Cross section of the buried object
ε	: Dielectric permittivity
ε_r	: Relative dielectric permittivity
σ	: Conductivity
μ	: Magnetic permeability
j	: Indice of illuminations
E	: Electric field
u	: scalar field function
k	: wavenumber
ω	: angular frequency
χ	: contrast function
Δ	: Laplace operator
$G\ \boldsymbol{x},\boldsymbol{y}$	: Green's function for Helmholtz equation
$\hat{G}$	: Fourier transform of G
δ	: Delta Dirac function
$G^{D,S}$	: Integral operators
ψ	: Spectral domain counterparts of G
I	: Identity operator
$\mathcal{L}$	: Integral operator
J_0	: Bessel function of the first kind
w	: Contrast source
F	: Cost functional
$\|\cdot\|$	: Euclidean norm
$\langle\ ,\ \rangle$	: Inner product
n	: Indice of iterations
ρ	: Data error
r	: Object error
v	: Update directions for iterations
α	: Step size for iterations
g	: Gradient of the cost functional
G^{S*},G^{D*}	: Adjoints of operators G^S,G^D
$\bar{G}$	: Complex conjugate of G
λ	: wavelength

η : noise level
r_d : uniformly distributed random variable

FIGURES

3D SCALAR IMAGING OF DIELECTRIC OBJECTS BURIED UNDER A ROUGH SURFACE

SUMMARY

Imaging of dielectric objects embedded in a layer, or beneath a rough surface is a popular subject of interest among remote sensing problems, and there are many studies that use microwaves for this purpose. In most of these studies, a rough surface separates two infinite half-spaces, and the object of interest lies in the inaccessible half-space. The area in which the object is presumed to be located is illuminated by transmitting antennas that are located in the accessible half-space, and the scattered field, which is the result of the interaction between the incident field and the irregularities in the medium, such as the unknown object and the layer it lies within, is measured by receiving antennas. The measured data is then used to obtain the unknown geometrical and material properties of the object. In the literature, the majority of the studies deal with layered media with planar interfaces, and 2D cases. Moreover, most of the studies on 3D cases dwell on only detection of dielectric objects, and very few deal with the imaging of dielectrics buried under a rough surface despite the importance of the problem from both theoretical and practical points of view. Nevertheless, none of these studies apply one of the well accepted nonlinear inversion techniques to a highly complicated case such as 3D case of imaging objects buried under a considerably rough surface, which is investigated here.

In this thesis, a nonlinear tomographic approach for a 3D scalar case of microwave imaging of dielectric objects buried under a rough surface is presented. First, the imaging problem is reduced to a system of two integral equations, which requires the Green's function of the background medium, including both the two half-spaces, and the rough surface. Therefore, the Green's function of the background is obtained numerically by using Buried Object Approach (BOA), which involves obtaining the Green's function of the two half-spaces with a planar interface, and then treating the roughness as a series of objects embedded in both half-spaces alternately. Then, the system of integral equations is solved for the contrast function via Contrast Source Inversion (CSI) method, which is one of the most successful nonlinear inversion techniques when the Green's function of the background is known. The efficiency of the method is tested numerically, and successful results are achieved for different frequencies, permittivity and conductivity values of both the medium and the object, different heights of the roughness, different size and depth of the object, and for cases of multiple objects.

ENGEBELİ YÜZEY ALTINA GÖMÜLÜ DİELEKTRİK CİSİMLERİN ÜÇ BOYUTLU SKALER DURUMDA GÖRÜNTÜLENMESİ

ÖZET

Bir katmana ya da engebeli bir yüzeyin altına gömülü dielektrik cisimlerin görüntülenmesi, uzaktan algılama konuları arasında önemli bir yer tutmaktadır. Bunun sebebi, tahribatsız kontrol, mayın tespit, yer altı boru ve tünellerinin incelenmesi, tıbbi görüntüleme, jeofizik veya arkeolojik etütler gibi geniş bir uygulama alanına sahip olmasıdır. Bu durumların çoğunda, iki katman ya da yarı uzay, engebeli bir yüzey tarafından ayrılır. Erişilemeyen katmanda bulunan ve hakkında nerede olabileceğinden başka bir şey bilinmeyen bir cisim, erişilebilen katmanda bulunan verici antenler tarafından aydınlatılır. Gelen alanın ortam ve içinde yer alan engebeli yüzey ile bilinmeyen cisim arasındaki etkileşiminden doğan saçılan alan ise alıcı antenler tarafından ölçülür. Bu şekilde elde edilen saçılan alan, cismin bilinmeyen yeri ve şekli gibi geometrik özellikleri ve dielektrik geçirgenliği ile iletkenliği gibi malzeme özelliklerinin elde edilmesinde kullanılır. Literatürde bu konuyu iki ve üç boyutta inceleyen pek çok çalışma bulunmaktadır. Bu çalışmalardan bazıları cisim ile engebeli yüzey arasındaki etkileşimleri incelemekle yetinirken, bazıları sadece engebeli yüzey, ya da sadece cisim üzerine odaklanarak iki aşamalı yaklaşımlara temel sağlamışlardır. Bu gibi yaklaşımlarda önce frekans ortalamalı Wigner-Ville fonksiyonu ile engebeli yüzey filtrelenir, ya da korelasyon yöntemi ile yüzey yaklaşık olarak tahmin edilir, daha sonra ise Newton-Kantorovitch gibi iteratif algoritmalar ile cisim tespit ve karakterize edilir. Bunun yanında, yeraltı radarı, dalgacık eşiği algoritması, Monte Carlo simülasyonları gibi yöntemler, engebeli yüzey ile cismi birlikte ele alır, ve cismin yerini tespit etmekte ya da cismin bulunduğu ve bulunmadığı durumları karşılaştırıp aradaki farkı farklı cisimler ile karşılaştırarak gömülü cismin ne olabileceğine ilişkin fikir vemekte kullanılır. Ancak bunlar günümüzün ihtiyaçlarını karşılamakta yetersizdir, ve cismin geometrik ve malzeme özelliklerini ortaya çıkarmak gibi karmaşık problemleri çözebilecek yöntemlere ihtiyaç duyulmaktadır. Bu yöntemler arasında, sığ ve mayın benzeri cisimleri görüntülemekte kullanılan sentetik açıklıklı radar, Green fonksiyonuna gerek duymayan lineer örnekleme, bir hata fonksiyonelini iteratif olarak minimize etmeye odaklananzamanda geri dönme, yarı analitik mod uydurma gibi yöntemler ya da zayıf bir saçıcının olması durumunda Born yaklaşıklığı ve buna eşlik eden ters Fourier dönüşümü veya tekil değer dekompozisyonu gibi yöntemler sayılabilir. Ancak bu yöntemlerin kullanıldığı çalışmaların çoğunda iki ortam arasındaki yüzeyin ya düz olduğu, ya da düz denebilecek kadar hafif bir engebeye sahip olduğu durum göz önüne alınmıştır. Oysa pratikte, görüntülenmek istenen cismin gömülü olduğu ortamın yüzeyi ihmal edilemeyecek derecede engebelidir, ve bu durum probleme ciddi güçlükler getirmektedir. Hem teorik, hem de pratik açıdan son derece önemli olmasına rağmen literatürde engebeli bir yüzey altına gömülü cisimlerin üç boyutta ele alındığı, ve hem geometrik, hem de malzeme özelliklerinin belirlenmeye çalışıldığı çalışmalar yok denecek kadar azdır. Buna ek olarak, geniş bir dielektrik

geçirgenliği aralığında, farklı geometrik özelliklere sahip saçıcıların görüntülenmesinde oldukça etkin olduğu bilinen doğrusal olmayan inversiyon yöntemlerinin engebeli yüzey altına gömülü dielektrik cisimlerin üç boyutlu durumda görüntülenmesi probleminde kullanıldığı bir çalışma, bildiğimiz kadarıyla bulunmamaktadır.

Bu tez çalışmasında, görüntülenmek istenen cismin arka planını teşkil eden uzaya ait Green fonksiyonunun bilinmesi halinde en etkili doğrusal olmayan inversiyon yöntemlerinden biri olarak kabul edilen Kontrast Kaynak İnversiyon (Contrast Source Inversion, CSI) yöntemi, engebeli bir yüzey altına gömülü dielektrik cisimlerin üç boyutlu durumda görüntülenmesi problemine uygulanmıştır. Bu amaçla, veri ve cisim denklemleri olarak adlandırılan, ve cismin dielektrik geçirgenliği ile iletkenliğini, cisim üzerinde bilinen sonlu bir uzayda alınan bir integral aracılığıyla sırasıyla ölçüm bölgesi ve cisim üzerindeki elektromanyetik alanlarla ilişkilendirilen Fredholm tipi integral denklemler yazılmıştır. Bu denklemlerin çekirdeğinde, engebeli yüzey de dahil olmak üzere cisim dışında kalan bütün yapıyı içeren uzaya ilişkin Green fonksiyonu yer almaktadır. Bu uzaya ilişkin Green fonksiyonununanalitik olarak hesaplanması mümkün olmamakla beraber, Gömülü Cisim Yaklaşımı (Buried Object Approach, BOA) olarak bilinen yöntem ile sayısal olarak elde edilebilir. Bu yaklaşıma göre engebeli yüzeyin girinti ve çıkıntıları, düzlemsel bir ara yüzle birbirinden ayrılmış iki parçalı uzaya gömülü cisimler olarak kabul edilir, ve ihtiyaç duyulan noktalara yerleştirilen noktasal kaynaklara ilişkin alanlar, Momentler Yöntemi (Method of Moments, MoM) ile sentetik olarak elde edilir. Bu alan büyüklükleri, Green fonksiyonunun aranan noktalardaki değerleridir. Arka planın Green fonksiyonunun hesaplanmasında gerekli olan iki parçalı uzaya ait Green fonksiyonu ise çekirdeğinde spektral yansıma ve iletim katsayılarının bulunduğu sonsuz integraller şeklinde yazılır, ve bu integraller sayısal olarak hesaplanır.

Böylece, cismin görüntülenmesi problemi, veri ve cisim denklemlerinden, cisim ile içinde bulunduğu ortamın dielektrik geçirgenlikleri ve iletkenlikleri arasındaki farkı ifade eden kontrast fonksiyonunun elde edilmesi olarak ifade edilen bir ters saçılma problemidir. Bu problem, kötü kurulmuş (ill-posed) ve doğrusal olmayan (nonlinear) bir problemdir, ve çözümü için kullanılabilecek bazı yaklaşıklıklara ve doğrusallaştırmalara dayalı yöntemler literatürde mevcuttur. Bu yöntemlerden biri olan Kontrast Kaynak İnversiyonu (CSI), doğrusal olmayan bir optimizasyon uygulamasıdır. Bunun için öncelikle sözü edilen integrallerin içinde çarpım halinde bulunan kontrast fonksiyonu ve alan ifadeleri, kontrast kaynağı adı verilen tek bir değişken olarak tanımlanır. Bu halde veri denklemi bu yeni değişkene göre doğrusal hale gelir, ancak denklemin kötü kurulmuş olması nedeniyle herhangi bir yöntemle kontrast kaynak için elde edilecek çözümün gerçekten farklı olması beklenir. Halbuki problem,denklem sisteminin asıl bilinmeyenleri olan kontrast fonksiyonu ve cisim üzerindeki alan açısından ele alındığında, cisim üzerindeki alanın kontrast fonksiyonuna bağlı olması nedeniyle problemin doğrusal olmayan bir problem olduğu görülür. Cismin zayıf bir saçıcı olması halinde problem, cismin üzerindeki toplam alanın gelen alana eşit kabul edildiği Born yaklaşıklığı kullanılarak doğrusal hale getirilebilir. Ancak geniş bir kompleks dielektrik sabiti ve cisim boyutu bölgesinde çözüm verebilecek bir görüntüleme yöntemi için problemin doğrusal olmayan doğasının göz ardı edilmemesi gerekir. Kontrast Kaynak İnversiyonu yönteminde herhangi bir doğrusallaştırma yapılmaz.Veri ile cisim denklemlerinin hatalarının toplamı şeklinde ifade edilenbir hata fonksiyoneli tanımlanır, vebu

fonksiyonel minimize edilecek şekilde kontrast kaynağı ve kontrast büyüklükleri dönüşümlü ve iteratif olarak güncellenir. Bu yöntem, iterasyonun her adımında düz problem çözümüne ihtiyaç duymaması, ve kontrast büyüklüğünün her adımda analitik olarak belirleniyor olması sebebiyle benzer yöntemlerden ayrılır.

Yöntemin verimini test etmek amacıyla çeşitli durumlar için simülasyonlar gerçekleştirilmiştir. Simülasyonlarda tek frekans kullanılmış, ve problemin üç boyutlu olmasından kaynaklanan hesaplama yükünü azaltmak amacıyla görüntüleme bölgesi, mümkün olduğunca küçük tutulmuştur. Bu şekilde farklı frekanslar, hem cisim, hem de içinde bulunduğu ortam için farklı dielektrik geçirgenlikleri ve iletkenlikler, farklı yapıdaki ve yükseklikteki engebeli yüzeyler, farklı boyutta ve derinliklerde bulunan cisimler, ve birden fazla cismi içeren çeşitli durumlar incelenmiştir. Bu incelemeler sonucunda, problemin yüksek karmaşıklıktaki doğasına rağmen, elde edilen sonuçların son derece tatmin edici olduğu, içinde bulunduğu ortamdan cismin net bir şekilde ayırdedilebildiği, ve malzeme özelliklerinin gerçeğe yakın olarak elde edilebildiği gözlemlenmiştir.

1. INTRODUCTION

1.1 Purpose of the Thesis

Microwave detection or imaging of objects embedded in a layer, or beneath a rough surface has been a popular subject of remote sensing due to its wide range of application areas such as nondestructive testing, mine detection, examination of underground pipes and tunnels, medical imaging, geophysical or archeological exploration.In most of these cases, a rough surface separatestwo layers, and the object of interest lies in the inaccessible layer beneath the rough surface, while the transmitting and receiving antennas lie in the accessible layer, above the surface. In order to image the object, a number of antennas illuminate the area in which the object is presumed to be located. Then, the scattered electromagnetic field, which arises from the interaction of the incident wave with the object and the layer it lies within, is measured by receiving antennas.The measured data is then used to obtain the unknown geometrical properties such as shape, location, and/or electromagnetic properties of the object, namely, dielectric permittivity and conductivity. Therefore, the purpose of this thesis is to give a fast and efficient methodology for determination of both geometrical and electromagnetic properties of dielectric objects buried under a rough surface.

1.2 Literature Review

There has been a wide range of approaches introduced to investigate, detect or image the rough surface that separates layered media, and objects buried in the inaccessible layer.[1] and [2] calculate and investigate the interactions between the object and a rough surface by using Forward-Backward (FB) method, and Propagation-Inside-Layer Expansion (PILE), respectively. The complexity observed in these studies led some researches to deal with roughness and object separately. For example, [3] focuses on the geometrical parameters of the layered media, such as rms height and correlation length, as well as the physical parameters, which are dielectric

permittivity and conductivity of each layer by minimizing the difference between the estimated and actual backscattering coefficients. Such reliable methods to estimate the profile of the roughness made two-step methods possible.In [4], for example, the object is detected by analyzing the frequency-averaged Wigner-Ville function to filter out rough surface scattering, and then the object is characterized by an iterative solution derived from the Newton-Kantorovitch algorithm. Moreover, [5] uses a correlation procedure of the scattered field in order to estimate the roughness profile, and then applies an iterative process based on a level-set formulation to obtain the shape of the buried object.

On the other hand, many researches choose to deal with the object and the rough profile of the layer they lie within, at the same time.Since the location of the object is unknown, and the layer it lies within is assumed infinite, detecting and locating the object is important. An application of angular correlation function to Ground Penetrating Radar (GPR) data to detect metallic objects, and a correlation of the scattered fields from two sets of data associated with two transmitters are given in [6], and [7], respectively, and [8] presents an image segmentation based on a wavelet thresholding algorithm applied to data gathered by Mid-Wavelength InfraRed (MWIR).Furthermore, Monte Carlo Simulations are applied to statistical average of Mueller and covariance matrix elements, which are obtained by simulations for rough ground with and without buried objects in [9], [10], respectively, whereas genetic and memetic algorithms use global optimization procedures [11-13].In addition, observing the surface impedance, which is obtained from the impedance boundary condition by using the electric field and its normal derivative on the surface [14], [15] reveals the location of the object.

However, reconstructing both geometrical and material properties of the object is more challenging, and several techniques have been applied to several data types throughout the years.Synthetic Aperture Radar (SAR) is used not only for imaging shallow buried landmine-like objects [16], but also for facilitating target identification by imaging different types of targets and obtaining a form of signature for them [17].Linear Sampling is used with reciprocity gap functional, avoiding the computation of the Green's function, which brings an undesirable computational cost [18], coupled with an analytic continuation [19].Furthermore, Time Reversal Method (TSM) focuses on minimizing a cost functional. It is used in [20] to synthesize a

wave that focuses on the scatterer by improving the signal-to-clutter ratio, and in [21] to image the rough surface first, under the assumption of free space, and then to estimate the object by using the surface obtained in the first step, in iterations in which both estimations are updated.In addition, Semi-Analytic Mode Matching (SAMM) is used in conjunction with least-squares [22], or with Levenberg-Marquardt algorithm, which uses a search direction between Gauss-Newton direction and the steepest descent direction, in order to minimize a cost functional representing the difference between estimated and real values of surface and constitutive parameters of both ground and object [23], iteratively.The efficiency of minimizing a cost functional depends on the choice of the step size and the direction, in which a closer estimate is searched. [24] presents use of Modified Gradient Method to reconstruct relative permittivity and conductivity maps within a search domain from the iterative minimization of a cost functional, which consists of the errors both in reproducing the data and the field inside this domain.

The nonlinear nature of the reconstruction process gives rise to a search for approximations suitable to the physical reality of the problems at hand. In case of a weak scatterer, whether it is the size of the object or the low contrast of its constitutive parameters to those of the background, Born approximation, which neglects the scattered field inside the object, is used. By linearizing the problem through Born approximation, [25] and [26] reconstruct the object using inverse Fourier transform, and Singular Value Decomposition (SVD), respectively, while [27] uses Born approximation for obtaining an initial estimate of the object in its iterative process. However, when the base requirements of the problem change due to its complexity, the approximations need to change as well. First and higher order extended Born approximations presented in [28] and [29], and distorted Born iterative methods presented in [30] and [31] are examples for such cases.

1.3 Significance of the Study

In this thesis, Contrast Source Inversion (CSI) is efficiently applied to the 3D scalar case of microwave imaging of buried dielectric objects under a rough surface for the first time. Since CSI, which is proven to be one of the most efficient nonlinear inversion techniques, requires the Green's function of the background medium, it is obtained numerically through the application of Buried Object Approach (BOA).

Therefore, the scalar Green's function of the two half-spaces with a planar interface is obtained as an infinite integral of spectral reflection and transmission coefficients, and the integrals are numerically calculated.Then, the contribution of the rough surface, which is assumed to be the field scattered by a series of objects buried in both half-spaces, is obtained by Method of Moments (MoM).

In spite of the incomplete data due to the nature of the subsurface imaging, and the complexity of the problem, as well as the high nonlinearity it holds, the proposed method yields remarkable results. The method is analyzed through several series of simulations in order to test the changes in several parameters of the configuration. The numerical results show that the method yields efficient results for a wide band of frequency, for a wide range of permittivity and conductivity values for both object and the background medium, for high roughnesses, small objects or multiple objects buried close to each other.

1.4 Organization of the Thesis

The organization of the thesis is as follows. The statement of the problem is given, and geometry and formulation are explained in Section 2. While the calculation of the Green's function of the background medium is given in Section 3, Section 4 is dedicated to the solution of the inverse problem. Several examples of numerical simulations are presented in Section 5, and finally, the conclusion is given in Section 6.

Throughout the thesis, the $\exp(-i\omega t)$ time factor is considered and suppressed.

2. STATEMENT OF THE IMAGING PROBLEM

2.1 Geometry of the Problem

The problem of the imaging of an unknown object, which lies beneath a rough surface, has been treated as a 3D scalar problem for computational simplicity. A cross section of the configuration can be seen in Figure 2.1. In this configuration, the two half-spaces are separated by a locally rough interface $\Gamma = f\ x_1, x_2$, where $f\ x_1, x_2$ is a single valued function [32], differing from the planar surface over a finite interval. The half-spaces $x_3 > f\ x_1, x_2$ and $x_3 < f\ x_1, x_2$ are composed of simple materials with constitutive parameters ε_1, σ_1 and ε_2, σ_2, respectively. In the lower half-space, an arbitrary shaped object with parameters $\varepsilon_{obj}, \sigma_{obj}$ is assumed to be located. All materials considered in this geometryare assumed to be nonmagnetic, with magnetic permeability equal to free-space permeability μ_0.
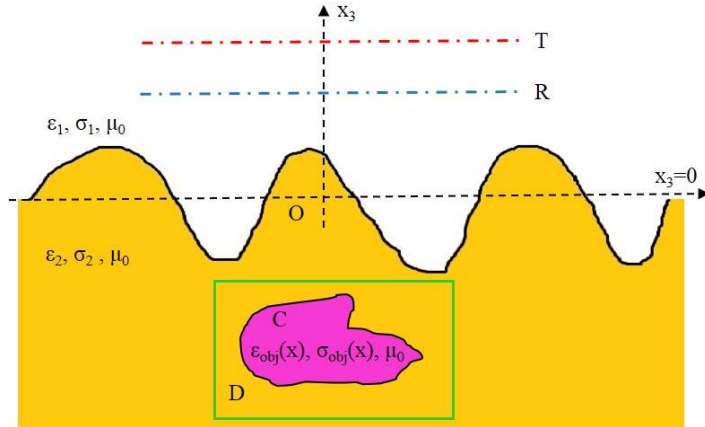
Figure 2.1: Cross section of the geometry of the problem

The region in which the object is assumed to be located is illuminated by microwave point sources at points z_j, $j = 1,2,\ldots,J$ on the surface T, and the total electric field $u_j\ \boldsymbol{x}\ = E_n\ \boldsymbol{x}; z_j$, where $\boldsymbol{x} = x_1, x_2, x_3$ is the position vector in $\mathbb{R}^3$, is measured by evenly spaced receivers located on the surface S for each illumination. Both surfaces T and S lie above the rough surface, parallel to the $x_3 = 0$ plane. The incident scalar

electric field function for each illumination is $E_i\left(\boldsymbol{x};z_j\right)=e^{ikr}\big/4\pi r$, which is time harmonic with angular frequency ω, and where r represents the distance between the source and the observation points. The inverse scattering problem here is reconstructing the unknown object's location, shape and constitutive parameters by using the total electric field $u_j\left(\boldsymbol{x}\right)=E_n\left(\boldsymbol{x};z_j\right)$, $n\in S$ measured on the surface S.

2.2 Formulation of the Problem

The total field $u_j\left(\boldsymbol{x}\right)$ can be considered as the sum of the *background field* $u_j^0\left(\boldsymbol{x}\right)$, the total field for the jth illumination in the absence of the object, and $u_j^s\left(\boldsymbol{x}\right)$, the field scattered by the object.

$$u_j\left(\boldsymbol{x}\right)=u_j^0\left(\boldsymbol{x}\right)+u_j^s\left(\boldsymbol{x}\right) \tag{2.1}$$

$u_j^0\left(\boldsymbol{x}\right)$ can be obtained by using a computational electromagnetics technique, in this case, BOA [33], which will be explained thoroughly in Section 3.1. In a source-free region, $u_j^0\left(\boldsymbol{x}\right)$ satisfies the homogeneous Helmholtz equation

$$\Delta u_j^0\left(\boldsymbol{x}\right)+k_b^2\left(\boldsymbol{x}\right)u_j^0\left(\boldsymbol{x}\right)=0 \tag{2.2}$$

where $k_b^2\left(\boldsymbol{x}\right)$ is the wavenumber of the background medium, whose square is given by

$$k_b^2\left(\boldsymbol{x}\right)=\begin{cases}k_1^2=\omega^2\varepsilon_1\mu_0+i\omega\sigma_1\mu_0, & x_3>f\left(x_1,x_2\right)\\ k_2^2=\omega^2\varepsilon_2\mu_0+i\omega\sigma_2\mu_0, & x_3<f\left(x_1,x_2\right)\end{cases} \tag{2.3}$$

Similarly, the total field $u_j\left(\boldsymbol{x}\right)$ satisfies

$$\Delta u_j\left(\boldsymbol{x}\right)+k^2\left(\boldsymbol{x}\right)u_j\left(\boldsymbol{x}\right)=0 \tag{2.4}$$

where $k^2\left(\boldsymbol{x}\right)$ is the wavenumber of the whole geometry, including the object, and given by

$$k^2\left(\boldsymbol{x}\right) = \begin{cases} \omega^2 \varepsilon_{obj} \mu_0 + i\omega\sigma_{obj}\mu_0, & \boldsymbol{x} \in C \\ k_b^2\left(\boldsymbol{x}\right), & \boldsymbol{x} \notin C \end{cases} \tag{2.5}$$

Finally, by adding the term $k_b^2\left(\boldsymbol{x}\right) u_j\left(\boldsymbol{x}\right) - k_b^2\left(\boldsymbol{x}\right) u_j\left(\boldsymbol{x}\right)$ to the left side of (2.4) and using (2.2) and (2.1), we obtain the equation

$$\Delta u_j^S\left(\boldsymbol{x}\right) + k_b^2\left(\boldsymbol{x}\right) u_j^S\left(\boldsymbol{x}\right) = -k_b^2\left(\boldsymbol{x}\right) \chi\left(\boldsymbol{x}\right) u_j\left(\boldsymbol{x}\right) \tag{2.6}$$

where $\chi\left(\boldsymbol{x}\right)$ is called the object function or contrast function, and defined by

$$\chi\left(\boldsymbol{x}\right) = \frac{k^2\left(\boldsymbol{x}\right)}{k_b^2\left(\boldsymbol{x}\right)} - 1 \tag{2.7}$$

Since the contrast function is a function of frequency, it will be different for all illuminations if they are performed in different frequencies. In order to avoid such complication throughout this thesis, all illuminations are considered to operate at a single frequency, and that is why, the index j is not used for the contrast χ.

In the inhomogeneous Helmholtz equation (2.6) that governs the propagation of the scattered field, the object is represented with the source term $-k_b^2\left(\boldsymbol{x}\right) \chi\left(\boldsymbol{x}\right) u_j\left(\boldsymbol{x}\right)$, and the scattered field $u_j^S\left(\boldsymbol{x}\right)$ is represented as a field radiating from this source in the medium defined by $k_b^2\left(\boldsymbol{x}\right)$ and also satisfies the Sommerfeld radiation condition

$$\lim_{r \to \infty} r^{1/2}\left(\frac{\partial u_j^S\left(\boldsymbol{x}\right)}{\partial r} - ik_b\left(\boldsymbol{x}\right) u_j^S\left(\boldsymbol{x}\right)\right) = 0, \qquad r = |x| \tag{2.8}$$

In general, the Sommerfeld radiation condition states that the enerty radiated from the sources must scatter to infinity [34]. This leads, in practice, to choosing the outgoing wave from possible solutions of the Helmholtz equation, and therefore ensuring the uniqueness of the solution to the scattering problem [35].

In order to solve the scattering problem given by the equations (2.6) and (2.8), one needs the Green's function of the background medium $G_b\left(\boldsymbol{x}, \boldsymbol{y}\right)$, which is defined as the total field due to a point source, which satisfies the differential equation

7

$$\Delta G_b\left(\boldsymbol{x},\boldsymbol{y}\right)+k_b^2\left(\boldsymbol{x}\right)G_b\left(\boldsymbol{x},\boldsymbol{y}\right)=-\delta\left(\boldsymbol{x}-\boldsymbol{y}\right) \qquad (2.9)$$

as well as the radiation condition. By using the Green's function $G_b\left(\boldsymbol{x},\boldsymbol{y}\right)$ as proven in [35], the scattered field $u_j^S\left(\boldsymbol{x}\right)$ that satisfies both (2.6) and (2.8) can be written in an integral form as

$$u_j^S\left(\boldsymbol{x}\right)=\iiint_C G_b\left(\boldsymbol{x},\boldsymbol{y}\right)k_b^2\left(\boldsymbol{y}\right)\chi\left(\boldsymbol{y}\right)u_j\left(\boldsymbol{y}\right)d\boldsymbol{y} \qquad (2.10)$$

Using this equation, the field scattered from the object can be calculated at any observation point x by integrating the source values y on the object. However, (2.10) shows that in order to obtain the scattered field at any point, the values of the total field u_j on the object are required. Since $u_j\left(\boldsymbol{x}\right)=u_j^0\left(\boldsymbol{x}\right)+u_j^S\left(\boldsymbol{x}\right)$ is valid at any point, we can write the equation

$$u_j\left(\boldsymbol{x}\right)=u_j^0\left(\boldsymbol{x}\right)+\iiint_C G_b\left(\boldsymbol{x},\boldsymbol{y}\right)k_b^2\left(\boldsymbol{y}\right)\chi\left(\boldsymbol{y}\right)u_j\left(\boldsymbol{y}\right)d\boldsymbol{y}, \quad \boldsymbol{x}\in C \qquad (2.11)$$

From (2.10) and (2.11), the scattered field at any point can be obtained by using Method of Moments (MoM) given in [36] for a known contrast function.

In the inverse scattering problem, on the other hand, the constitutional parameters as well as the location C of the object are unknown, while the total field $u_j\left(\boldsymbol{x}\right)$, and therefore $u_j^S\left(\boldsymbol{x}\right)$ on the measurement points on the surface S are known. Since the contrast function χ in (2.7) vanishes for $\boldsymbol{x}\notin C$, we perform the integrations in (2.10) and (2.11) on a reconstruction domain D which is large enough to contain the unknown object as shown in Figure 2.1. In this case, the total field u_j that appears in the integrals is redefined for $\boldsymbol{x}\in D$, and the resulting integral equations can be symbolically written as

$$u_j=u_j^0+G^D\chi u_j, \quad \boldsymbol{x}\in D, \quad j=1,2,...,J \qquad (2.12)$$

$$u_j^S=G^S\chi u_j, \quad \boldsymbol{x}\in S, \quad j=1,2,...,J \qquad (2.13)$$

8

where G^D and G^S are integral operatorsmapping from $L^2 \ D \ $ to $L^2 \ D \ $ and $L^2 \ D \ $ to $L^2 \ S \ $, respectively, and given by

$$G^{D,S}\psi \ \ x \ = \iiint\limits_D G_b \ \ x,y \ k_b^2 \ \ y \ \psi \ \ y \ dy, \quad x \in D,S \qquad (2.14)$$

Equations (2.12) and (2.13) are known as the *object* and *data* equations, respectively, and the imaging problem at hand can be expressed as the reconstruction of χ from these equations since its real and imaginary parts are related to the dielectric permittivity $\varepsilon_{obj} \ x \ $, and the conductivity $\sigma_{obj} \ x \ $ of the object. This problem is nonlinear with respect to χ, and the ContrastSource Inversion (CSI) method [37] given in Section 4 is used to solve it.

3. THE GREEN'S FUNCTION OF THE BACKGROUND MEDIUM

3.1 Buried Object Approach

Solving the inverse scattering problem given by (2.12) and (2.13) requires the Green's function of the background, $G_b(x, y)$ for necessary pairs of x and y. In this study, this is achieved by Buried Object Approach (BOA), which considers the roughness as a series of scatterers whose constitutive parameters differ according to their position. The parameters of the sections B_1, B_3,... B_{2N-1}, that lie in the $x_3 < 0$ half space and the sections B_2, B_3,... B_{2N} that lie in the $x_3 > 0$ region which are shown in Figure 3.1 are ε_1, σ_1 and ε_2, σ_2, respectively.
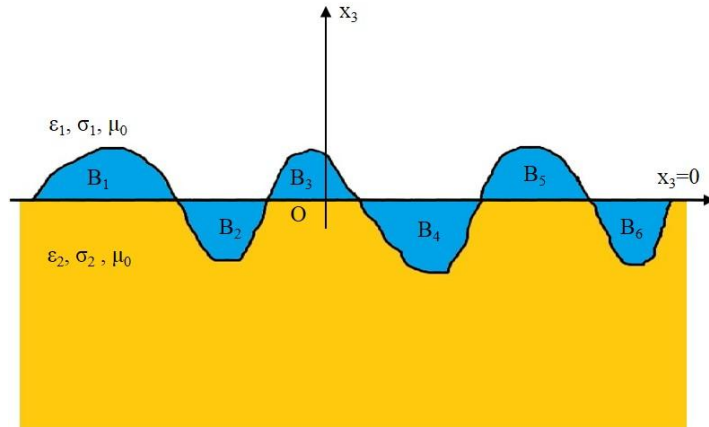
Figure 3.1: Cross-sectional representation of the geometry according to the BOA.

$G_b(x, y)$, the Green's function of the background can be expressed as the sum of the contributions of its two components,

$$G_b(x, y) = G_S(x, y) + G_0(x, y) \tag{3.1}$$

where $G_0(x, y)$ is the Green's function of the two-part space with a planar interface, and $G_S(x, y)$ is the contribution of the roughness. $G_S(x, y)$ can also be considered as the field scattered from the objects that form the roughness due to a point source with unit strength and is located at y, and $G_0(x, y)$ and $G_b(x, y)$ are the incident and total

11

fields, respectively. In this case, the integral equation of such a scattering problem can be written as

$$(I - \mathcal{L}) G_S(\mathbf{x}, \mathbf{y}) = \mathcal{L} G_0(\mathbf{x}, \mathbf{y}) \tag{3.2}$$

where the integral operator $\mathcal{L}$ is defined by

$$\mathcal{L} G(\mathbf{x}, \mathbf{y}) = \iiint_C G_0(\mathbf{x}, \mathbf{z}) \left[k_b^2(\mathbf{z}) - k_0^2(\mathbf{z}) \right] G(\mathbf{z}, \mathbf{y}) \, d\mathbf{z} \tag{3.3}$$

In (3.3), $k_0(\mathbf{z})$ is the wave number of the two-part space with planar interface, and its square is defined as

$$k_0^2(\mathbf{z}) = \begin{cases} k_1^2(\mathbf{z}), & x_2 > 0 \\ k_2^2(\mathbf{z}), & x_2 < 0 \end{cases} \tag{3.4}$$

Equation (3.2) can be solved for $G_S(\mathbf{x}, \mathbf{y})$ by using the forward solution procedure given in [36].

3.2 Green's Function of the Two Half-Spaces with a Planar Interface

In order to solve (3.2), $G_0(\mathbf{x}, \mathbf{y})$, which can be considered as the total field due to a point source of unit strength that is located at $\mathbf{y}$ in the two-part space with a planar interface. The geometry in question is shown in Figure 3.2.

$G_0(\mathbf{x}, \mathbf{y})$ satisfies the Helmholtz equation

$$\Delta G_0(\mathbf{x}, \mathbf{y}) + k_0^2(\mathbf{x}) G_0(\mathbf{x}, \mathbf{y}) = -\delta(\mathbf{x} - \mathbf{y}) \tag{3.5}$$

and the boundary conditions at $x_3 = 0$

$$\begin{aligned} G_0|_{x_2=0+\xi} &= G_0|_{x_2=0-\xi}, & \xi \to 0 \\ \frac{\partial G_0}{\partial x_3}\Big|_{x_2=0+\xi} &= \frac{\partial G_0}{\partial x_3}\Big|_{x_2=0-\xi}, & \xi \to 0 \end{aligned} \tag{3.6}$$

as well as the Sommerfeld radiation condition.
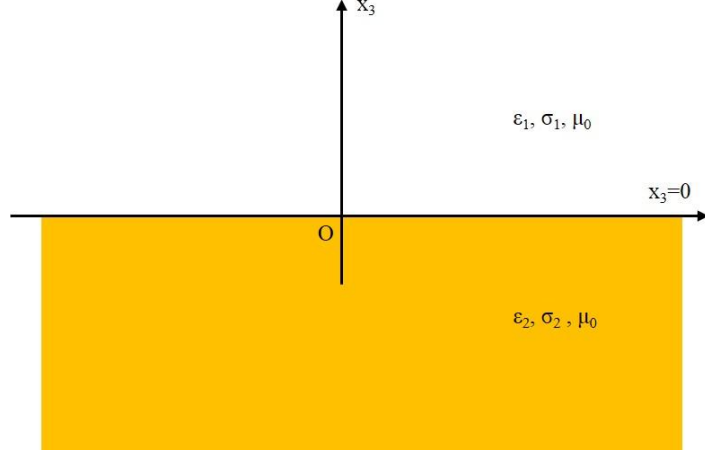
Figure 3.2: Cross-section of two half-spaces with a planar interface

Having the discontinuity of the geometry in the Ox_3-direction, we take the Fourier transform of (3.5) twice, with respect to x_1, and x_2, so that we deal with the problem only in the Ox_3-direction. Thus, we obtain

$$\frac{\partial^2 \hat{G}_0}{\partial x_3^2} - \left(\upsilon_1^2 + \upsilon_2^2 - k_0^2 \right) \hat{G}_0 = -e^{-i\upsilon_1 y_1} e^{-i\upsilon_2 y_2} \delta\left(x_3 - y_3 \right) \qquad (3.7)$$

where $\hat{G}_0$ is the double Fourier transform of G_0 defined by

$$\hat{G}_0\left(\upsilon_1, \upsilon_2, x_3; \boldsymbol{y} \right) = \int\limits_{-\infty}^{\infty} \int\limits_{-\infty}^{\infty} G_0\left(x_1, x_2, x_3; \boldsymbol{y} \right) e^{-i\upsilon_1 x_1} e^{-i\upsilon_2 x_2} dx_1 d x_2 \qquad (3.8)$$

In this case, $\hat{G}_0$ satisfies the boundary conditions at $x_3 = 0$, which are given in (3.6),

$$\begin{aligned} \hat{G}_0 \Big|_{x_2 = 0+\xi} &= \hat{G}_0 \Big|_{x_2 = 0-\xi}, & \xi \to 0 \\ \frac{\partial \hat{G}_0}{\partial x_3} \bigg|_{x_2 = 0+\xi} &= \frac{\partial \hat{G}_0}{\partial x_3} \bigg|_{x_2 = 0-\xi}, & \xi \to 0 \end{aligned} \qquad (3.9)$$

and also the boundary conditions at $x_3 = y_3$, which are

$$\begin{aligned} \hat{G}_0 \Big|_{x_2 = y_2+\xi} &= \hat{G}_0 \Big|_{x_2 = y_2-\xi}, & \xi \to 0 \\ \frac{\partial \hat{G}_0}{\partial x_3} \bigg|_{x_2 = y_2+\xi} - \frac{\partial \hat{G}_0}{\partial x_3} \bigg|_{x_2 = y_2-\xi} &= -e^{-i\upsilon_1 y_1} e^{-i\upsilon_2 y_2}, & \xi \to 0 \end{aligned} \qquad (3.10)$$

(3.7) can be solved for $\hat{G}_0$ by using (3.9), (3.10), and the Sommerfeld radiation condition, and after applying the inverse Fourier transform, which is defined by

$$G_0\ x_1, x_2, x_3; \boldsymbol{y}\ = \left(\frac{1}{2\pi}\right)^2 \int_{-\infty}^{\infty}\int_{-\infty}^{\infty} \hat{G}_0\ \upsilon_1, \upsilon_2, x_3; \boldsymbol{y}\ e^{i\upsilon_1 x_1} e^{i\upsilon_2 x_2} d\upsilon_1 d\upsilon_2 \qquad (3.11)$$

the Green's function of the two-part space with planar interface G_0 can be found as

$$G_0\ \boldsymbol{x}, \boldsymbol{y}\ = \begin{cases} G_1\ \boldsymbol{x}, \boldsymbol{y}\ G_2\ \boldsymbol{x}, \boldsymbol{y}\ , & x_3 > 0, y_3 > 0 \\ G_3\ \boldsymbol{x}, \boldsymbol{y}\ , & x_3 < 0, y_3 > 0 \\ G_4\ \boldsymbol{x}, \boldsymbol{y}\ , & x_3 > 0, y_3 < 0 \\ G_1\ \boldsymbol{x}, \boldsymbol{y}\ G_5\ \boldsymbol{x}, \boldsymbol{y}\ , & x_3 < 0, y_3 < 0 \end{cases} \qquad (3.12)$$

where G_1 is the direct part while $G_{2,5}$ and $G_{3,4}$ are the reflected and transmitted parts of the Green's function. G_1 can be written as

$$G_1 = \frac{e^{ik_0|\boldsymbol{x}-\boldsymbol{y}|}}{4\pi|\boldsymbol{x}-\boldsymbol{y}|} \qquad (3.13)$$

.

On the other hand, there are no explicit expressions for $G_{2,3,4,5}$, that is why they are obtained by taking the inverse double Fourier transform of

$$G_2 = \frac{1}{4\pi}\int_0^\infty \frac{R_{12}}{\gamma_1} k_\rho J_0\ k_\rho|x_\rho - y_\rho|\ e^{-\gamma_1\ x_3+y_3}\ dk_\rho, \qquad x_3 > 0, y_3 > 0$$

$$G_3 = \frac{1}{4\pi}\int_0^\infty \frac{T_{12}}{\gamma_1} k_\rho J_0\ k_\rho|x_\rho - y_\rho|\ e^{-\gamma_1 y_3 + \gamma_2 x_3} dk_\rho, \qquad x_3 < 0, y_3 > 0$$

$$\qquad (3.14)$$

$$G_4 = \frac{1}{4\pi}\int_0^\infty \frac{T_{21}}{\gamma_2} k_\rho J_0\ k_\rho|x_\rho - y_\rho|\ e^{-\gamma_1 x_3 + \gamma_2 y_3} dk_\rho, \qquad x_3 > 0, y_3 < 0$$

$$G_5 = \frac{1}{4\pi}\int_0^\infty \frac{R_{21}}{\gamma_2} k_\rho J_0\ k_\rho|x_\rho - y_\rho|\ e^{\gamma_2\ x_3+y_3}\ dk_\rho, \qquad x_3 < 0, y_3 < 0$$

where

$$|x_\rho - y_\rho| = \sqrt{x_1 - y_1^{\ 2} + x_2 - y_2^{\ 2}} \qquad (3.15)$$

14

$$R_{12} = \frac{\gamma_1 - \gamma_2}{\gamma_1 + \gamma_2}, \qquad T_{12} = \frac{2\gamma_1}{\gamma_1 + \gamma_2}$$

$$R_{21} = \frac{\gamma_2 - \gamma_1}{\gamma_1 + \gamma_2}, \qquad T_{12} = \frac{2\gamma_2}{\gamma_1 + \gamma_2}$$

(3.16)

and

$$\gamma_1 = \sqrt{\upsilon^2 - k_1^2}, \qquad \gamma_2 = \sqrt{\upsilon^2 - k_2^2} \text{ , where } \upsilon^2 = \upsilon_1^2 + \upsilon_2^2 \qquad (3.17)$$

The square root functions in (3.17) are defined on the complex υ-plane under the conditions

$$\gamma_q \ \upsilon \ = -ik_q, \qquad q = 1, 2 \qquad (3.18)$$
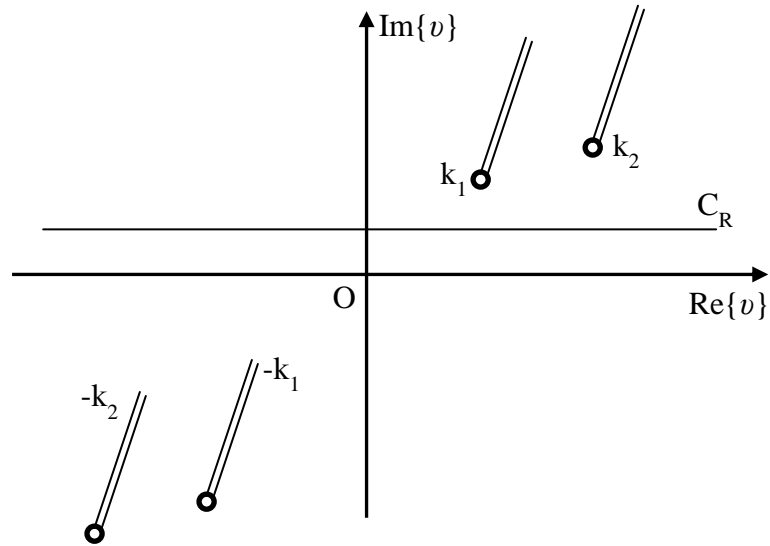
Figure 3.3: The integration path of the infinite integral on complex domain.

4. SOLUTION OF THE INVERSE SCATTERING PROBLEM

4.1 Properties of the Inverse Scattering Problem

Jacques Hadamard defined mathematical models of physical phenomena as *well-posed* problem if they satisfy three conditions such as a solution exists, the solution is unique, and the solution's behavior changes continuously with the initial conditions [38]. If at least one of these conditions are not satisfied, the problem is defined as *ill-posed*. The problem defined in (2.10) and (2.11) is well-posed as shown in [35], which means that the scattered field for a known object exists, is unique, and continuously depends on the constitutive parameters of the object. However,an inverse problem, involves reconstructing the material properties of an unknown object by using a scattered field obtained through a finite number of measurements under a finite number of illuminations, and realistically contaminated by noise.Although the data equation is linear with respect to the product of χu, which are both unknown, it is highly nonlinear with respect to the contrast function χ, which is the main focus of the inverse problem because u itself depends on χ.

The nonlinearity can be seen by rewriting (2.12) in the inverse form as

$$u_j = \left(I - G^D \chi \right)^{-1} u_j^0 \tag{4.1}$$

where *I* is the identity operator, and by substituting it into (2.13)

$$u_j^S = G^S \left[\chi \left(I - G^D \chi \right)^{-1} u_j^0 \right]. \tag{4.2}$$

Several methods deal with this nonlinearity through different approximations. For example, in case of a weak scatterer, whether it is the size, or the values of its constitutive parameters, approximating the inverse operator by

$$\left(I - G_j^D \chi \right)^{-1} \approx I \tag{4.3}$$

In other words, neglecting the contribution of the scatterer to the total field and assuming $u_j = u_j^0$ leads to Born approximation, and through this approximation, the data equation in (4.2) will be linear.On the other hand, in iterative methods where χ_n is reconstructed, approximations are made considering the iteration steps, such as

$$I - G_j^D \chi_n^{-1} \approx I - G_j^D \chi_{n-1}^{-1} \tag{4.4}$$

leads to the iterative Born method [39], and linearization of

$$I - G_j^D \chi_n^{-1} \approx \left[I - G_j^D \chi_{n-1} - G_j^D \chi_n - \chi_{n-1} \right]^{-1} \tag{4.5}$$

using $\Delta\chi_n = \chi_n - \chi_{n-1}$, namely,

$$I - G_j^D \chi_n^{-1} \approx \left[I + I - G_j^D \chi_{n-1}^{-1} G_j^D \Delta\chi_n \right] I - G_j^D \chi_{n-1}^{-1} \tag{4.6}$$

to the Newton-Kantorovich method [40,41]. While these iterative methods require direct scattering problem to be solved at each iterative step, Contrast Source Inversion method, which is the main component of this study, focuses on minimizing a cost functional that consists of normalized data and object errors without solving the direct problem.

4.2 Solution of the Inverse Scattering Problem via the CSI

Since the total field u and the contrast function χ appear as a product in data and object equations, the quantity

$$w_j = \chi u_j \tag{4.7}$$

which is called a contrast source, is introduced, since u_j satisfies the Helmholtz equation

$$\nabla^2 + k^2 \ u_j = -k^2 w_j \quad \text{in C.} \tag{4.8}$$

Using (4.7), the data equation becomes

$$f_j = G_j^S w_j, \qquad j = 1, 2, ..., J \tag{4.9}$$

And the object equation becomes

$$\chi u_j^{inc} = w_j - \chi G_j^D w_j, \qquad j = 1, 2, ..., J \tag{4.10}$$

Therefore, the cost functional which CSI intends to minimize can be defined as

$$F = \frac{\sum_j \left\| f_j - G_j^S w_j \right\|_S^2}{\sum_j \left\| f_j \right\|_S^2} + \frac{\sum_j \left\| \chi u_j^{inc} - w_j + \chi G_j^D w_j \right\|_D^2}{\sum_j \left\| \chi u_j^{inc} \right\|_S^2} \tag{4.11}$$

where $\left\| \cdot \right\|_S^2$ and $\left\| \cdot \right\|_D^2$ represent the norms on $L_2 \; S$ and $L_2 \; D$, respectively, and they are defined as

$$\left\| u_j \right\|_{D,S} = \left\langle u_j, u_j \right\rangle_{D,S}^{1/2} \tag{4.12}$$

and

$$\left\langle u_j, v_j \right\rangle_{D,S} = \int_{D,S} u_j \; \boldsymbol{x} \; \bar{v}_j \; \boldsymbol{x} \; d\boldsymbol{x} \tag{4.13}$$

where the overbar denotes complex conjugate. The first term of the cost functional represents the error in the data equations in (4.9), and the second term represents the error in the object equations in (4.10) for each illumination. The normalization of the two terms is carried out so that both terms would be equal to one if $w_j = 0$. As mentioned in [37], the iterations will be carried out in two main steps. First, the contrast sources w_j^n will be constructed by using the Conjugate Gradient (CG) method so that they would minimize the whole cost functional, and then by using the updated value of w_j^n, the object function χ^n will be determined to minimize the second part of the cost functional. The process will continue in the following manner, until the difference between the cost functionals of two consecutive iterations go below a predetermined value:

The data and object errors are defined as

$$\rho_{j,n} = f_{j,n} - G_j^S w_{j,n} \tag{4.14}$$

$$r_{j,n} = \chi_n u_{j,n} - w_{j,n} \tag{4.15}$$

respectively, where

$$u_{j,n} = u_j^0 + G_j^D w_{j,n} \tag{4.16}$$

If $w_{j,n-1}$ and χ_{n-1} are known, then w_j is updated as

$$w_{j,n} = w_{j,n-1} + \alpha_{j,n} v_{j,n} \tag{4.17}$$

where the step sizes $\alpha_{j,n}$ are constants, and the update directions $v_{j,n}$ are functions of position.

The update directions $v_{j,n}$ are chosen to be the Polak-Ribière conjugate gradient directions, and defined as

$$
\begin{aligned}
v_{j,0} &= 0 \\
v_{j,n} &= g_{j,n} + \frac{\left\langle g_{j,n}, g_{j,n} - g_{j,n-1} \right\rangle_D}{\left\langle g_{j,n-1}, g_{j,n-1} \right\rangle_D} v_{j,n-1}, n \geq 1
\end{aligned}
\tag{4.18}
$$

where $g_{j,n}$ is the gradient (Frechet derivative) of the cost functional with respect to w_j evaluated at $w_{j,n-1}$, χ_{n-1}, and can be expressed as

$$g_{j,n} = -\frac{G_j^{S*} \rho_{j,n-1}}{\sum_k \|f_k\|_S^2} - \frac{r_{j,n-1} G_j^{D*} \ \overline{\chi}_{n-1} r_{j,n-1}}{\sum_k \|\chi_{n-1} u_k^{inc}\|_D^2} \tag{4.19}$$

where G_j^{S*} and G_j^{D*} are adjoints of G_j^S and G_j^D mapping $L_2 \ S$ into $L_2 \ D$ and $L_2 \ D$ into $L_2 \ D$, respectively, and they are defined as

$$G_j^{D*} v_j = \iint_D \overline{G} \ y; x \ v_j \ y \ dy, \qquad x \in D \tag{4.20}$$

and

$$G_j^{S*} v_j = \iint_S \bar{G}\left(\boldsymbol{y};\boldsymbol{x}\right) v_j\left(\boldsymbol{y}\right) d\boldsymbol{y}, \qquad \boldsymbol{x} \in D \tag{4.21}$$

After determining the update directions $v_{j,n}$, the step size $\alpha_{j,n}$ is determined to minimize the cost functional $F\left(w_{j,n-1} + \alpha_{j,n} v_{j,n}\right)$ in an explicit form

$$
\begin{aligned}
F &= \frac{\sum_j \left\| f_j - G_j^S w_{j,n} \right\|_S^2}{\sum_j \left\| f_j \right\|_S^2} + \frac{\sum_j \left\| \chi_{n-1} u_{j,n} - w_{j,n} \right\|_D^2}{\sum_j \left\| \chi_{n-1} u_j^{inc} \right\|_D^2} \\
&= \frac{\sum_j \left\| \rho_{j,n-1} - \alpha_{j,n} G_j^S v_{j,n} \right\|_S^2}{\sum_j \left\| f_j \right\|_S^2} + \frac{\sum_j \left\| r_{j,n-1} - \alpha_{j,n}\left(v_{j,n} - \chi_{n-1} G_j^D v_{j,n}\right) \right\|_D^2}{\sum_j \left\| \chi_{n-1} u_j^{inc} \right\|_D^2}
\end{aligned}
\tag{4.22}
$$

and is obtained as

$$
\begin{aligned}
\alpha_{j,n} =& \left(\frac{\left\langle \rho_{j,n-1}, G_j^S v_{j,n} \right\rangle_S}{\sum_j \left\| f_j \right\|_S^2} + \frac{\left\langle r_{j,n-1}, v_{j,n} - \chi_{n-1} G_j^D v_{j,n} \right\rangle_D}{\sum_j \left\| \chi_{n-1} u_j^{inc} \right\|_D^2} \right) \\
&\times \left(\frac{\left\| G_j^S v_{j,n} \right\|_S^2}{\sum_k \left\| f_k \right\|_S^2} + \frac{\left\| v_{j,n} - \chi_{n-1} G_j^D v_{j,n} \right\|_D^2}{\sum_k \left\| \chi_{n-1} u_k^{inc} \right\|_D^2} \right)^{-1}
\end{aligned}
\tag{4.23}
$$

After $w_{j,n}$ is obtained, the total field $u_{j,n}$ inside D can be updated using (4.16) and (4.17) as

$$u_{j,n} = u_{j,n-1} + \alpha_{j,n} G_j^D v_{j,n} \tag{4.24}$$

In the second part of an iteration, the contrast χ, which minimizes the second term of the cost functional

$$F_D = \frac{\sum_j \left\| \chi_n u_{j,n} - w_{j,n} \right\|_D^2}{\sum_j \left\| \chi_n u_{j,n} \right\|_D^2} \tag{4.25}$$

is to be found. However, as presented in [37], using simpler functional

$$F'_D = \sum_j \left\| \chi_n u_{j,n} - w_{j,n} \right\|_D^2 \tag{4.26}$$

instead of (4.25) would lead to guarantee that the process is always error reducing, and allows easy implementation of *a priori* information or constraints on χ. Equation (4.26) can be rewriten as

$$
\begin{aligned}
F'_D &= \sum_j \int_D \left\{ \left[\frac{\mathrm{Re}\ w_{j,n}\bar{u}_{j,n}}{|u_{j,n}|} - \chi^r |u_{j,n}| \right]^2 + \left[\frac{\mathrm{Im}\ w_{j,n}\bar{u}_{j,n}}{|u_{j,n}|} - \chi^i |u_{j,n}| \right]^2 \right\} d\upsilon \\
&= \int_D \left\{ \left[\chi^r \left(\sum_j |u_{j,n}|^2 \right)^{1/2} - \frac{\sum_j \mathrm{Re}\ w_{j,n}\bar{u}_{j,n}}{\left(\sum_j |u_{j,n}|^2 \right)^{1/2}} \right]^2 \right. \\
&\quad + \left[\chi^i \left(\sum_j |u_{j,n}|^2 \right)^{1/2} - \frac{\sum_j \mathrm{Im}\ w_{j,n}\bar{u}_{j,n}}{\left(\sum_j |u_{j,n}|^2 \right)^{1/2}} \right]^2 + \sum_j \left(\frac{\mathrm{Re}\ w_{j,n}\bar{u}_{j,n}}{|u_{j,n}|} \right)^2 \\
&\quad - \frac{\left[\sum_j \mathrm{Re}\ w_{j,n}\bar{u}_{j,n} \right]^2}{\sum_j |u_{j,n}|^2} + \sum_j \left(\frac{\mathrm{Im}\ w_{j,n}\bar{u}_{j,n}}{|u_{j,n}|} \right)^2 - \left. \frac{\left[\sum_j \mathrm{Im}\ w_{j,n}\bar{u}_{j,n} \right]^2}{\sum_j |u_{j,n}|^2} \right\} d\upsilon
\end{aligned}
\tag{4.27}
$$

Without any *a priori* information on χ, F'_D can be minimized by choosing

$$
\chi_n^r = \frac{\sum_j \mathrm{Re}\ w_{j,n}\bar{u}_{j,n}}{\sum_j |u_{j,n}|^2} \qquad \chi_n^i = \frac{\sum_j \mathrm{Im}\ w_{j,n}\bar{u}_{j,n}}{\sum_j |u_{j,n}|^2}
\tag{4.28}
$$

If we have *a priori* information that χ^r and χ^i are positive, which for the application at hand they are, then using this information to write (4.27) as

$$
\begin{aligned}
F'_D &= \int_D \left\{ \chi^r \left(\left[\chi^{r\frac{1}{2}} \left(\sum_j |u_{j,n}|^2 \right)^{\frac{1}{2}} - \frac{1}{\chi^{r\frac{1}{2}}} \left(\sum_j \left(\frac{\mathrm{Re}\ w_{j,n}\bar{u}_{j,n}}{|u_{j,n}|} \right)^2 \right)^{\frac{1}{2}} \right]^2 \right. \right. \\
&\quad + 2 \left(\sum_j |u_{j,n}|^2 \right)^{\frac{1}{2}} \left[\sum_j \left(\frac{\mathrm{Re}\ w_{j,n}\bar{u}_{j,n}}{|u_{j,n}|} \right)^2 \right]^{\frac{1}{2}} - 2\sum_j \mathrm{Re}\ w_{j,n}\bar{u}_{j,n} \cdots \right)
\end{aligned}
$$

22

$$+ \chi^{i} \left[\left[\chi^{i\frac{1}{2}} \left(\sum_{j} |u_{j,n}|^2 \right)^{\frac{1}{2}} - \frac{1}{\chi^{i\frac{1}{2}}} \left(\sum_{j} \left(\frac{\mathrm{Im}\ w_{j,n}\overline{u}_{j,n}}{|u_{j,n}|} \right)^2 \right)^{\frac{1}{2}} \right]^2 \right.$$

$$+ 2 \left(\sum_{j} |u_{j,n}|^2 \right)^{\frac{1}{2}} \left[\sum_{j} \left(\frac{\mathrm{Im}\ w_{j,n}\overline{u}_{j,n}}{|u_{j,n}|} \right)^2 \right]^{\frac{1}{2}} - 2\sum_{j} \mathrm{Im}\ w_{j,n}\overline{u}_{j,n} \left. \right\} dv \qquad (4.29)$$

Although the first option that comes to mind to minimize F'_{D} is choosing χ^{r} and χ^{i} to be zero, the appearance of $1/\chi^{i1/2}$ and $1/\chi^{r1/2}$ in this expression makes it unreasonable. Furthermore, we can see from (4.26) that $\chi \neq 0$ whenever $w_{j} \neq 0$ .Therefore, since the Schwarz inequality ensures that

$$\left(\sum_{j} |u_{j,n}|^2 \right)^{\frac{1}{2}} \left[\sum_{j} \left(\frac{\mathrm{Re}\ w_{j,n}\overline{u}_{j,n}}{|u_{j,n}|} \right)^2 \right]^{\frac{1}{2}} - \sum_{j} \mathrm{Re}\ w_{j,n}\overline{u}_{j,n} \geq 0 \qquad (4.30)$$

And

$$\left(\sum_{j} |u_{j,n}|^2 \right)^{\frac{1}{2}} \left[\sum_{j} \left(\frac{\mathrm{Im}\ w_{j,n}\overline{u}_{j,n}}{|u_{j,n}|} \right)^2 \right]^{\frac{1}{2}} - \sum_{j} \mathrm{Im}\ w_{j,n}\overline{u}_{j,n} \geq 0 \qquad (4.31)$$

χ^{r} and χ^{i} are chosen to minimize the factors multiplying χ^{r} and χ^{i} , as

$$\chi_{n}^{r} = \left\{ \frac{\sum_{j} \mathrm{Re}\ w_{j,n}\overline{u}_{j,n} \left/ |u_{j,n}|^2 \right.}{\sum_{j} |u_{j,n}|^2} \right\}^{\frac{1}{2}} \qquad \chi_{n}^{i} = \left\{ \frac{\sum_{j} \mathrm{Im}\ w_{j,n}\overline{u}_{j,n} \left/ |u_{j,n}|^2 \right.}{\sum_{j} |u_{j,n}|^2} \right\}^{\frac{1}{2}} \qquad (4.32)$$

If further information on χ^{r} or χ^{i} is known *a priori*, then this known value can be used in equations (4.28) or (4.32) for further restriction of the reconstruction during the iterations.

Using the path we take during this procedure leads us to a reasonable choice of the starting values of $w_{j,0}$. Observing from (4.11) that starting iterations with $w_{j,0} = 0$

would cause $\chi_0^r = \chi_0^i = 0$, and and the cost functional would be undefined. Therefore, the values

$$w_{j,0}^{bp} = \frac{\left\| G_j^{S*} f_j \right\|_D^2}{\left\| G_j^S G_j^{S*} f_j \right\|_S^2} G_j^{S*} f_j \tag{4.33}$$

that are obtained by backpropagation are chosen. This completes the CSI procedure.

5. NUMERICAL SIMULATIONS

In order to test the efficiency of the method, several numerical simulations have been performed for various cases. Throughout the simulations, all materials are assumed to be nonmagnetic, with free-space magnetic permeability μ_0. The upper half-space $x_3 > 0$ is assumed to be free-space, and unless otherwise stated, the lower half-space $x_3 < 0$ is assumed to be dry soil, with constitutive parameters $\varepsilon_{rsoil} = 3.6$ and $\sigma_{soil} = 10^{-4}$. Equally spaced point sources and measurement points are located on surfaces, whose area are defined by $-0.5\lambda_{soil} < x_1 < 0.5\lambda_{soil}$ and $-0.5\lambda_{soil} < x_2 < 0.5\lambda_{soil}$, in the upper half-space, $0.2\lambda_{soil}$ and $0.1\lambda_{soil}$ above the maximum height of the roughness, respectively.

The scattered field data are obtained synthetically by solving the direct scattering problem given by (3.1) and (3.2) for an object buried under a rough surface via Method of Moments (MoM), using Buried Object Approach (BOA) given in sections 2 and 3. In order to avoid inverse crime, cubical cells of size $\lambda_{soil}/30 \times \lambda_{soil}/30 \times \lambda_{soil}/30$ are used for the production of the scattered field, while the Green's function which is used in the inversion procedure is calculated for a reconstruction domain consisting of larger cells. 5% random noise $\eta|u_{s,j}|e^{i2\pi r_d}$, is added to the scattered field, where η is the noise level, and r_d is a uniformly distributed random variable between 0 and 1, and therefore the corresponding signal-to-noise ratio is $SNR = -20\log_{10}\eta$. At each simulation, the iterative process is performed by considering the positivity constraint for the contrast, and stopped at 500 iterations. The reconstruction results are given in their own color scales since using the same color scale for both the original and reconstructed profiles may not be enough for visual interpretation when the values are underestimated.

For the first set of simulations, the rough surface shown in Figure 5.1 is considered. The roughness covers a $1.7\lambda_{soil} \times 1.7\lambda_{soil}$ area in x_1x_2 plane, and the height, the difference between its maximum and minimum values on x_3 axis is $0.2\lambda_{soil}$. A

sphericalobject with a $0.125\lambda_{soil}$ radius,dielectric permittivity $\varepsilon_{obj} = 5\varepsilon_0$ and conductivity $\sigma_{obj} = 0.01$ is centeredat $0,0,-0.275\lambda_{soil}$. The configuration is illuminated by 16 point sources operating at different frequencies, changing between 100MHz to 3 GHz, for each example, and the scattered field is measured at 64 points. The inversion procedure is carried out in a reconstruction domain consisting of cubical cells of size $\lambda_{soil}/25$ on each side.

The first example is carried out at 100 MHz frequency. The profile of the real and reconstructed values in the cross-section at $x_1 = 0$ of the reconstruction domain are given in Figure 5.2. Figure 5.2 (a) and (c) show that the profile of the reconstructed relative dielectric permittivity of the domain is very well determined, and the shape and the location of the object is clear, although the object looks slightly bigger than its real size. Similarly, the conductivity profile of the domain that can be seen in Figure 5.2 (b) and (d) shows that the reconstructed value is very close to the real value, and location of the object is very clear, but it looks smaller than it really is.

For the second example is carried out at 300 MHz frequency. Figure 5.3 shows the real and reconstructed values of both relative permittivity and conductivity profile of the reconstruction domain, at $x_1 = 0$. The reconstructed values of both are very well determined, and the shape and location of the object are distinctive. However, in both Figure 5.3 (c) and (d), the object seems slightly mislocated, and it looks bigger than its real size in (c) while it looks smaller in (d).
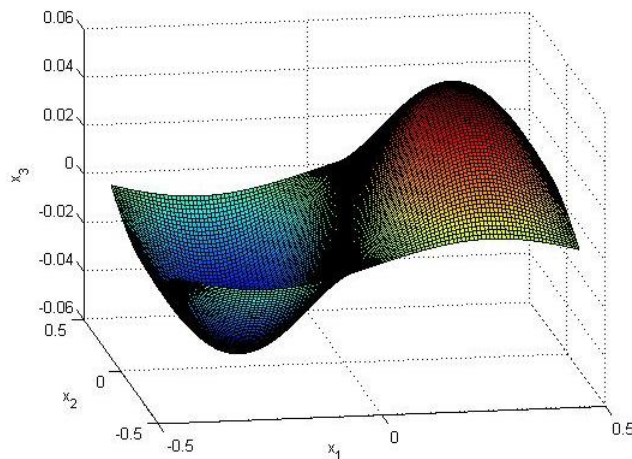
**Figure 5.1:**Rough surface profile for the first set of simulations that are investigated through Figure 5.2-5.7
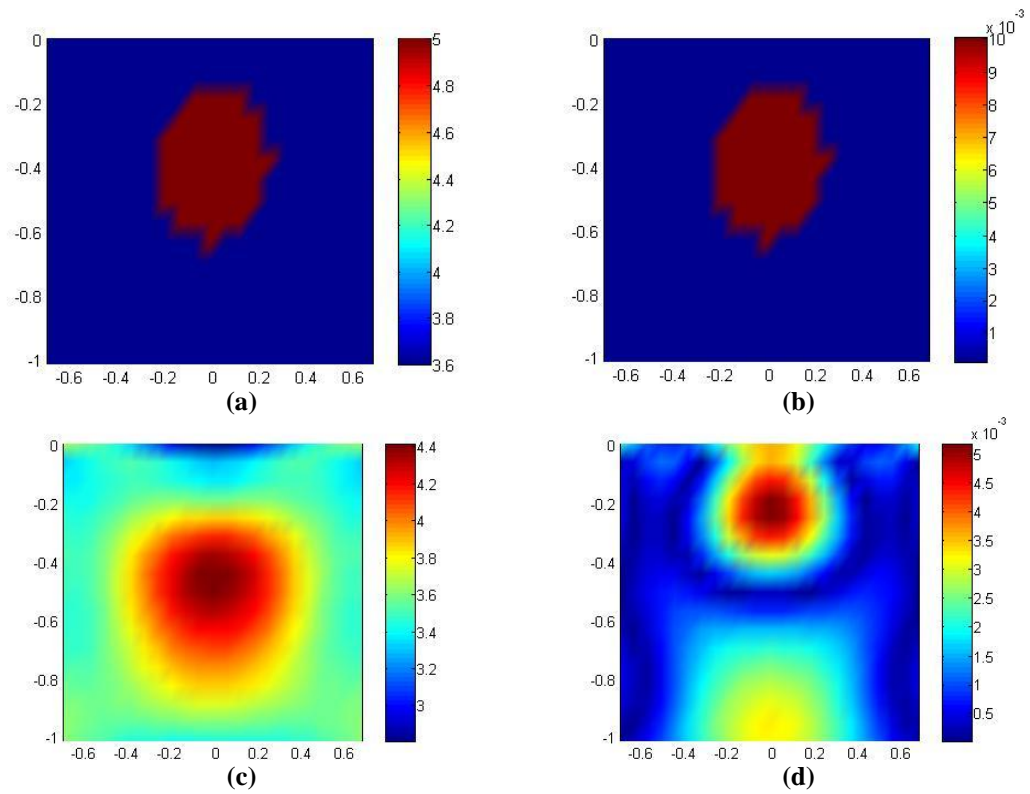
Figure 5.2:(a) Original relative dielectric permittivity **(b)**Original conductivity **(c)** Reconstructed relative dielectric permittivity **(d)** Reconstructed conductivity profile at x$_1$=0 for frequency test atf = 100 MHz.
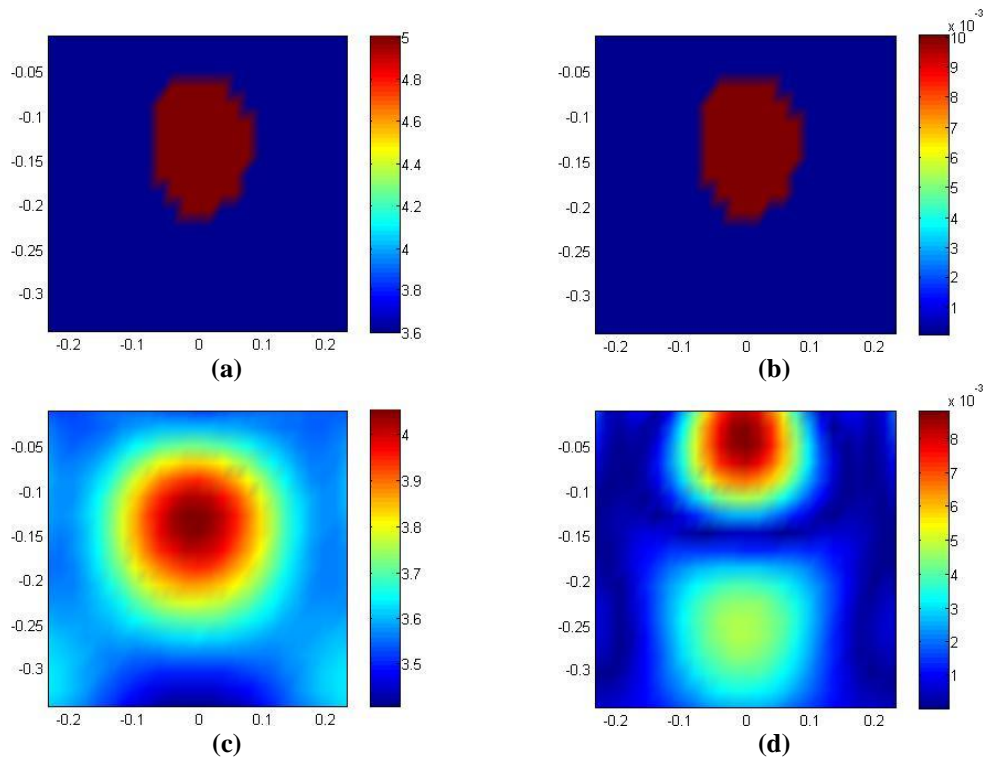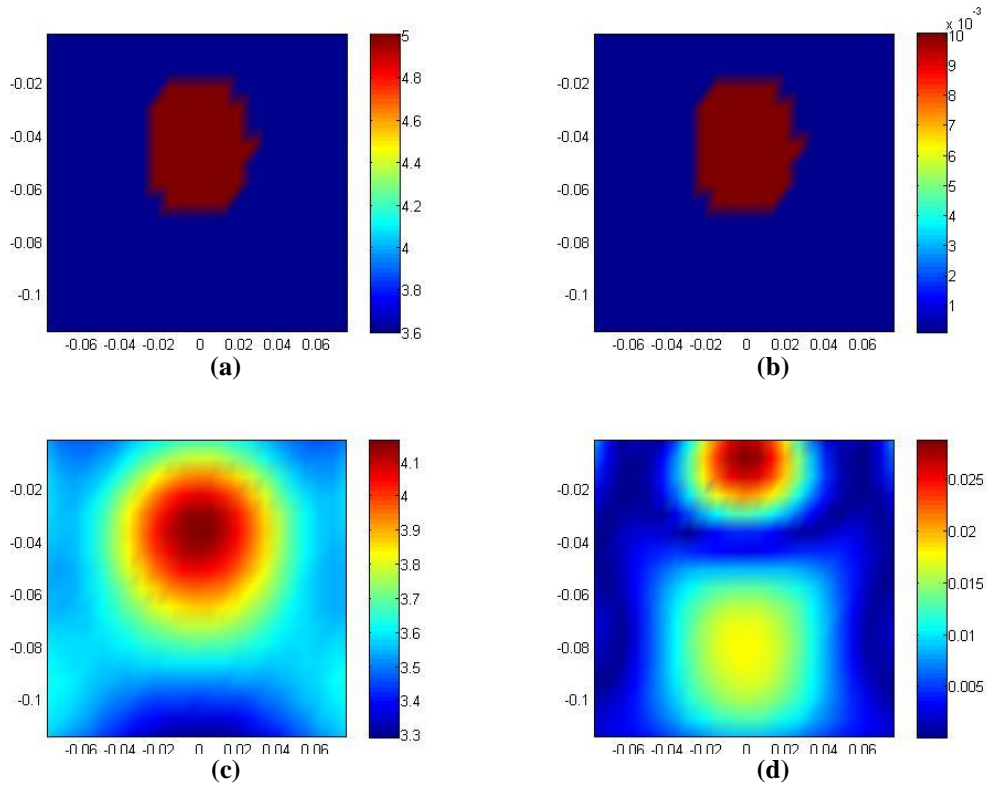

Figure 5.3:(a) Original relative dielectric permittivity **(b)**Original conductivity **(c)** Reconstructed relative dielectric permittivity **(d)** Reconstructed conductivity profile at x$_1$=0 for frequency test at f = 300 MHz.

Figure 5.4 shows the results of the third example, ran at 600 MHz operating frequency. The reconstructed values of both relative permittivity and conductivity shown in (c) and (d), respectively, are close to the real ones shown in (a) and (b), but the reconstructed value of conductivity is slightly over its real value. Although the shape and location of the object seen in Figure 5.4 (c) is very clear and matches the real one, only the upper part of the object seems distinct in the conductivity profile in Figure 5.4 (d).

The results of the fourth example, which was ran at 900 MHz frequency can be seen in Figure 5.5. As it was in the previous example, the values in the reconstructed relative dielectric permittivity profile in Figure 5.5 (c) are close to the real ones in Figure 5.5 (a), and both the shape and the location of the object are clear and matches the real profile. However, the values in the reconstructed conductivity profile in Figure 5.5 (d) are higher than the real values shown in Figure 5.5 (b), and again, only the top of the object seems distinct.
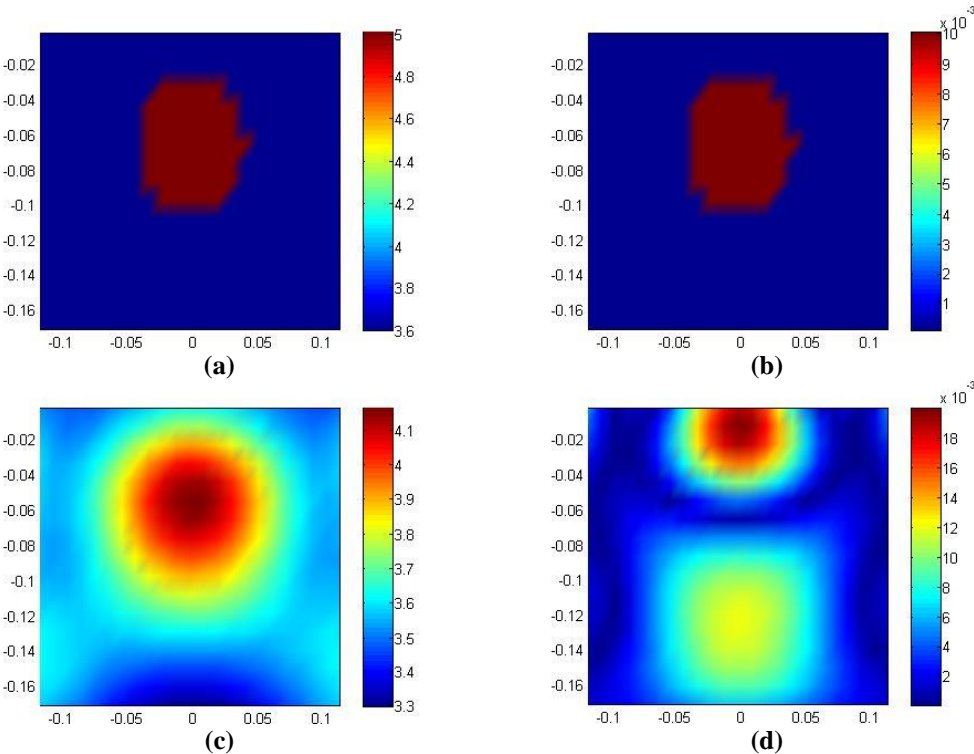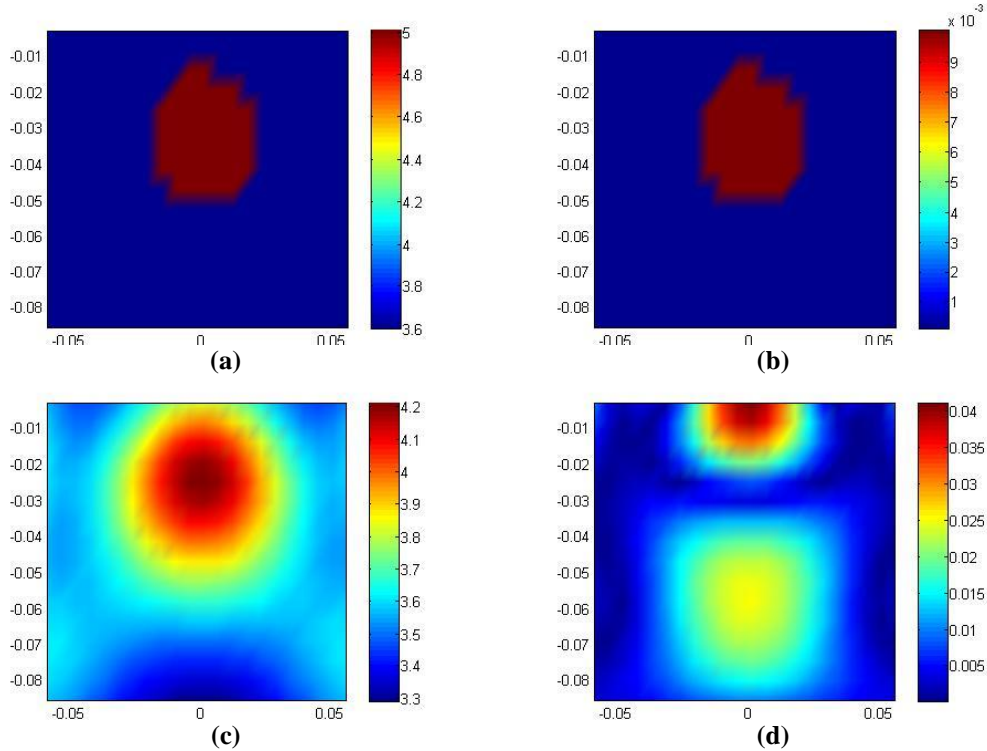

Figure 5.4:(a) Original relative dielectric permittivity **(b)**Original conductivity **(c)** Reconstructed relative dielectric permittivity **(d)** Reconstructed conductivity profile at $x_1=0$ for frequency test at f = 600 MHz.
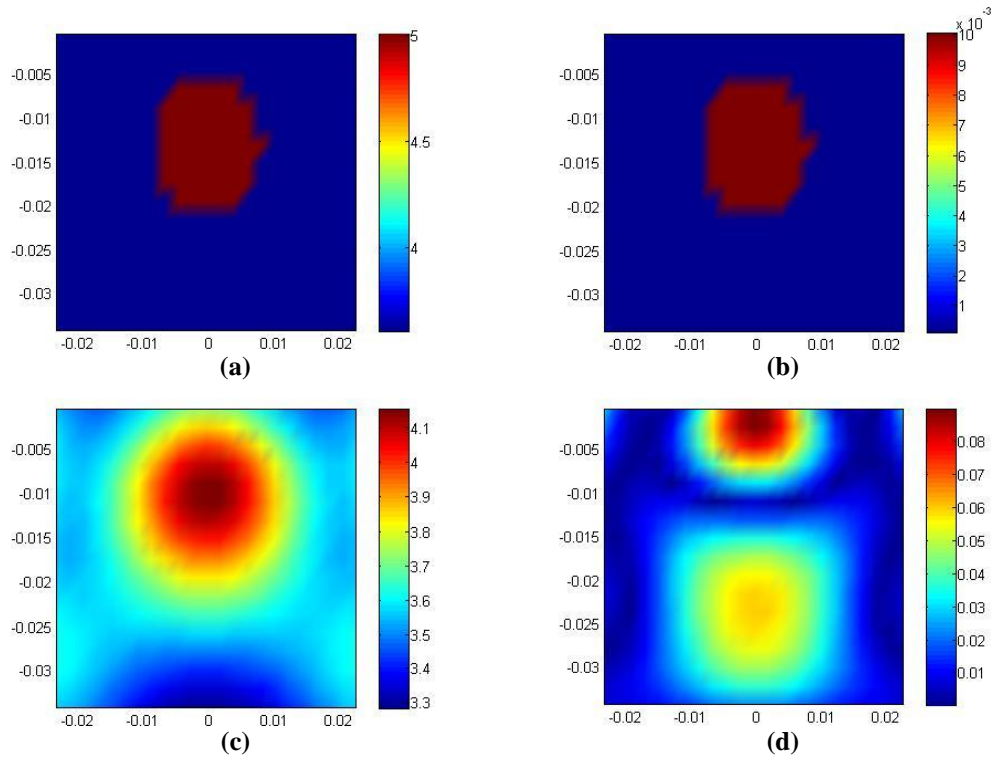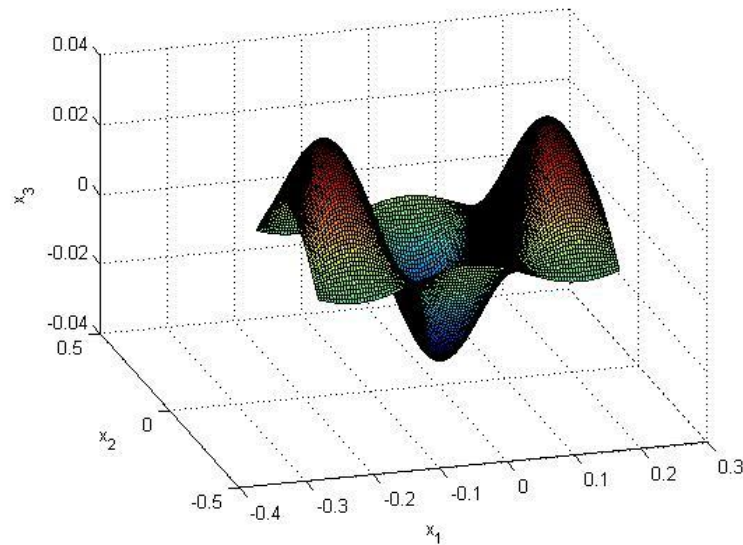
Figure 5.5:(a) Original relative dielectric permittivity **(b)**Original conductivity **(c)** Reconstructed relative dielectric permittivity **(d)** Reconstructed conductivity profile at x_1=0 for frequency test at f = 900 MHz.

Figure 5.6:(a) Original relative dielectric permittivity **(b)**Original conductivity **(c)** Reconstructed relative dielectric permittivity **(d)** Reconstructed conductivity profile at x_1=0 for frequency test at f = 1.2 GHz.

Figure 5.7:(a) Original relative dielectric permittivity **(b)**Original conductivity **(c)** Reconstructed relative dielectric permittivity **(d)** Reconstructed conductivity profile at $x_1=0$ for frequency test at f = 3 GHz.

The results of the fifth and the sixth examples that are shown in Figure 5.6 and Figure 5.7, respectively, are in line with the ones in the previous example. While the real and reconstructed relative permittivity profiles in (a) and (c) in both figures match, the values seen in Figure 5.6 (d) and Figure 5.7 (d) are higher than the real ones in Figure 5.6 (b) and Figure 5.7 (b), and although the object is detectable, only the top of the objects seem visible in both figures.

The first set of simulations, which are performed at operating frequencies from 100 MHz to 3 GHz, show that the method is very effective for reconstructing the relative dielectric permittivity profile of the domain, considering boththe values in the profile, and the distinctivity of the shape and location of the object.However, when the reconstructed values of the conductivity in the domain are considered, although the simulations performed at lower frequencies yield satisfactory results, the values reconstructed at higher frequencies exceed the real values in the profile. Furthermore, although the object looks slightly misplaced in the conductivity profiles at lower frequencies, they are sufficiently distinctive, but at higher frequencies, only the top of the object seems visible.

For the second set of simulations, the $0.2\lambda_{soil}$ high rough surface, which lies in $-0.85\lambda_{soil} \leq x_1 \leq 0.85\lambda_{soil}$, $-0.85\lambda_{soil} \leq x_2 \leq 0.85\lambda_{soil}$, $-0.1\lambda_{soil} \leq x_3 \leq 0.1\lambda_{soil}$, is considered, and shown in Figure 5.8. Circular objects with a radius of $0.125\lambda_{soil}$, having different constitutive paramters at each example, are centered at $0, 0, -0.35\lambda_{soil}$. 16 source an 64 measurement points are used in the simulations, and the inversion is carried out in a reconstruction domain which consists of cubical cells of size $\lambda_{soil} / 24$ on each side.

The effect of the object's conductivity is investigated in the next three simulations, by using objects with the same dielectric permittivity, but different conductivities. First example is carried out with an object with relative permittivity $\varepsilon_{obj} = 7\varepsilon_0$, and conductivity $\sigma_{obj} = 0.05$. The real and reconstructed profiles of permittivity, which can be seen in Figure 5.9 (a) and (c), respectively, show that the reconstructed values are close to the real ones, and the shape and location of the object are clear. Furthermore, the conductivity of the object is successfully estimated, and the top of the object is visible in Figure 5.9 (d), hence the location of the object is also clear.

Figure 5.8: Rough surface profile for the simulations whose results are shown through Figure 5.9-5.21
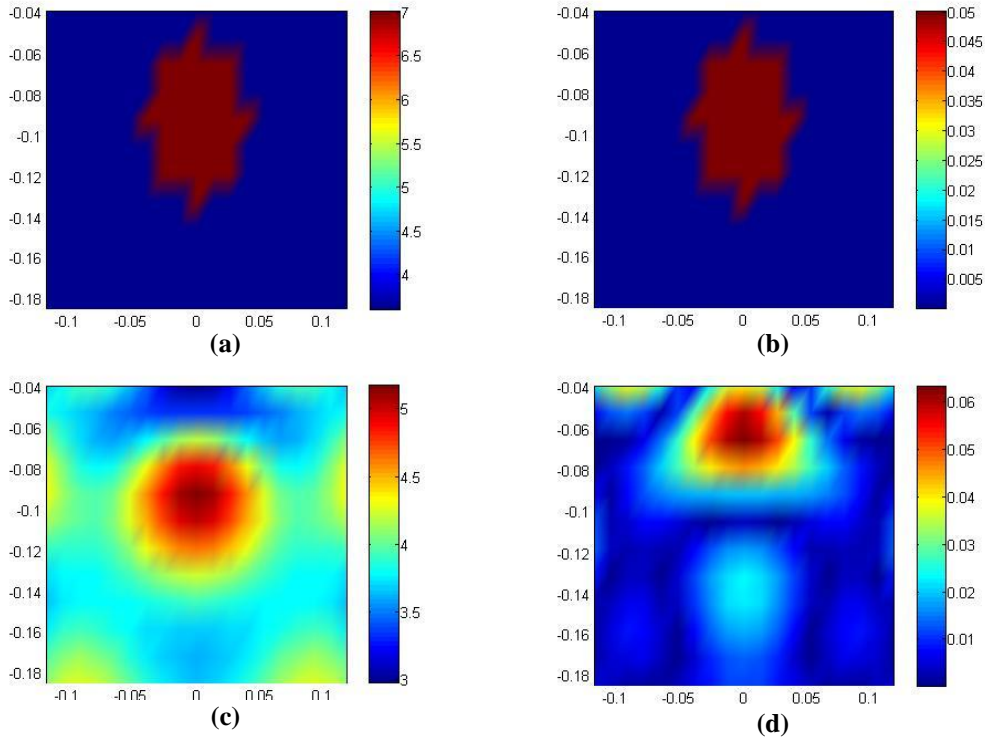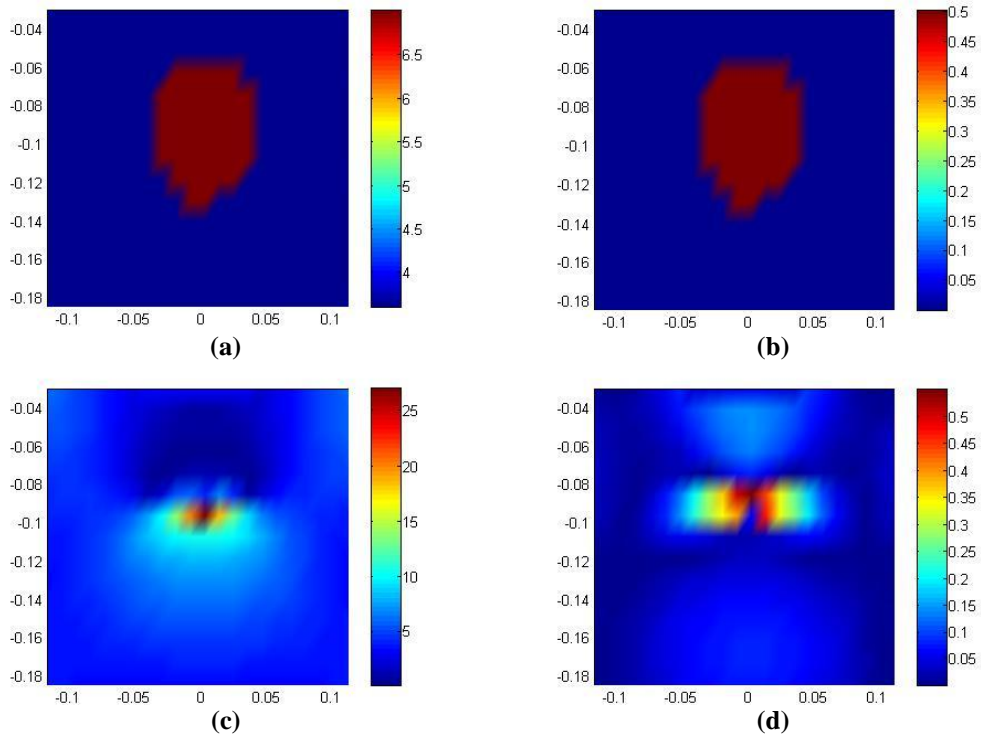
Figure 5.9:(a) Original relative dielectric permittivity **(b)**Original conductivity **(c)** Reconstructed relative dielectric permittivity **(d)** Reconstructed conductivity profile at $x_1=0$ for conductivity test for an object with $\varepsilon_{obj}=7\varepsilon_0$, $\sigma_{obj}=0.05$.
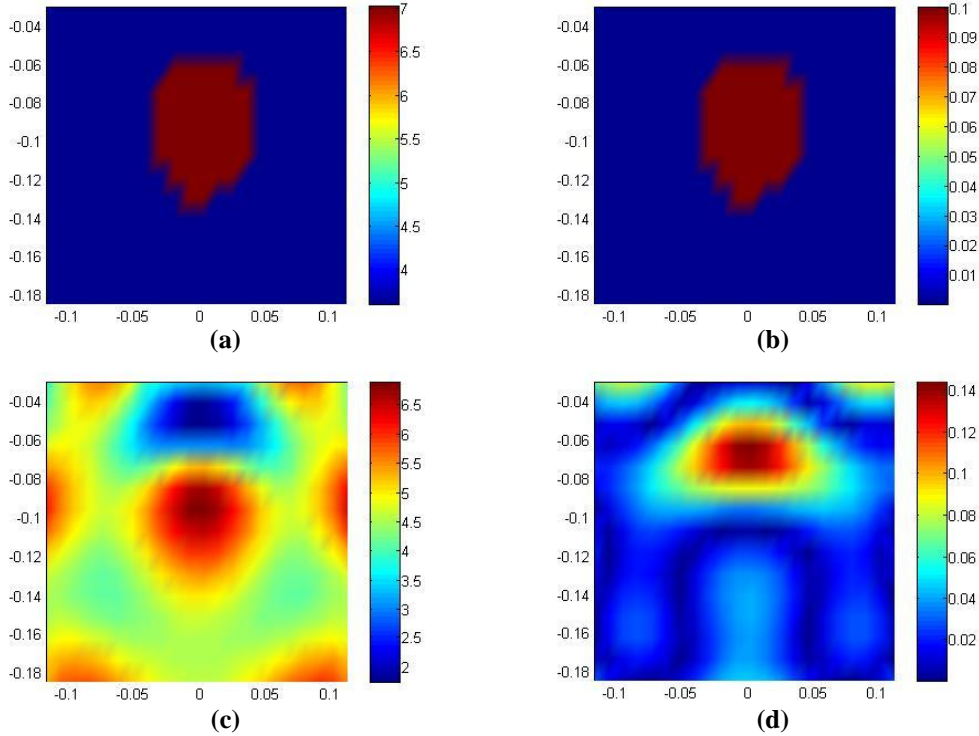
Figure 5.10:(a) Original relative dielectric permittivity **(b)**Original conductivity **(c)** Reconstructed relative dielectric permittivity **(d)** Reconstructed conductivity profile at $x_1=0$ for conductivity test for an object with $\varepsilon_{obj}=7\varepsilon_0$, $\sigma_{obj}=0.1$.

In the next example, an object with the same permittivity as the previous one, and a conductivity of $\sigma_{obj} = 0.1$ is used, and the real and reconstructed profiles are shown in Figure 5.10. It is observed that the shape and location of the object are clear in Figure 5.10 (c), and the values are estimated very well. On the other hand, in Figure 5.10 (d), the values of the conductivity profile are slightly overestimated, but the top of the object is visible; therefore, the location of the object is clear. However, the object having a relatively high conductivity increases the problem's nonlinearity, and causes some reflections on both profiles.

Figure 5.11:(a) Original relative dielectric permittivity **(b)**Original conductivity **(c)** Reconstructed relative dielectric permittivity **(d)** Reconstructed conductivity profile at $x_1=0$ for conductivity test for an object with $\varepsilon_{obj}=7\varepsilon_0$, $\sigma_{obj}=0.5$.

Another object, with the same dielectric permittivity, $\varepsilon_{obj} = 7\varepsilon_0$, but a higher conductivity, $\sigma_{obj} = 0.5$ is used in the next example, whose simulation results can be seen in Figure 5.11.The reconstructed profiles of both relative permittivity and conductivity in Figure 5.11 (c) and (d), respectively, show the location of the object clearly, but the shape of the object is not recognizable. The relative permittivity of the object is overestimated in Figure 5.11 (c), while the value of the conductivity is estimated exactly as the real value in Figure 5.11 (d), which suggests that the high value of the conductivity dominates the contrast of the object, leading to a highly

nonlinear problem, and favouring the conductivity in the inversion of the contrast function.

The simulations of the next three examples, whose results are shown through Figures 5.12 - 5.14, are performed to observe the change in relative permittivity of the object. In each of them, objects with the same conductivity, $\sigma_{obj} = 0.001$, but different permittivities, changing from 5 to 20 are used. Figure 5.12 (a) and (c) show the real and reconstructed profiles of relative dielectric permittivity for the first example, in which an object with a permittivity $\varepsilon_{obj} = 5\varepsilon_0$ is used. Reconstructed permittivity profile shows a close estimate of the values inside the object, and its shape and location are perfectly recovered. Moreover, Figure 5.12 (d) shows the location of the object clearly although only the top of the object is visible, and the values are overestimated.

Similarly, an object with $\varepsilon_{obj} = 10\varepsilon_0$ is used in the next example. Similar to the previous example, the values of the reconstructed permittivity profile in Figure 5.13 (c) are very close to the ones of the real profile in Figure 5.13 (a), and the shape and location of the object is perfectly reconstructed. However, the object in the conductivity profile Figure 5.13 (d) is not recognizable, and its value is overestimated.

(a)

(b)

(c)

(d)
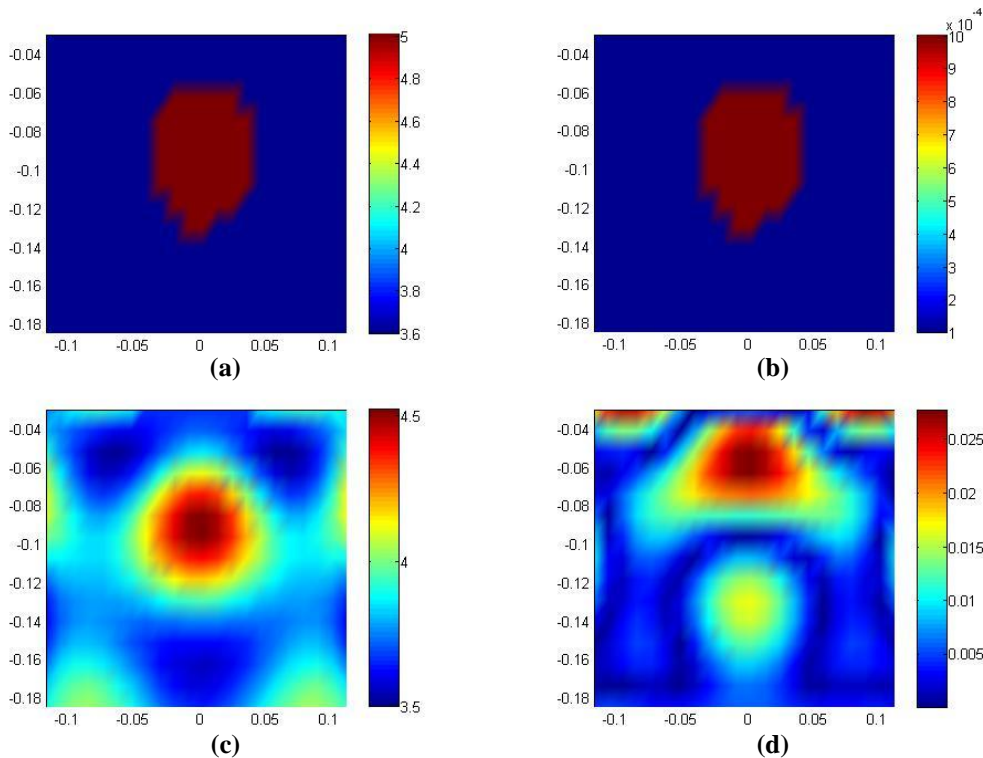
Figure 5.12:(a) Original relative dielectric permittivity **(b)**Original conductivity **(c)** Reconstructed relative dielectric permittivity **(d)** Reconstructed conductivity profile at $x_1=0$ for permittivity test for an object with $\varepsilon_{obj}=5\varepsilon_0$, $\sigma_{obj}=10^{-3}$.
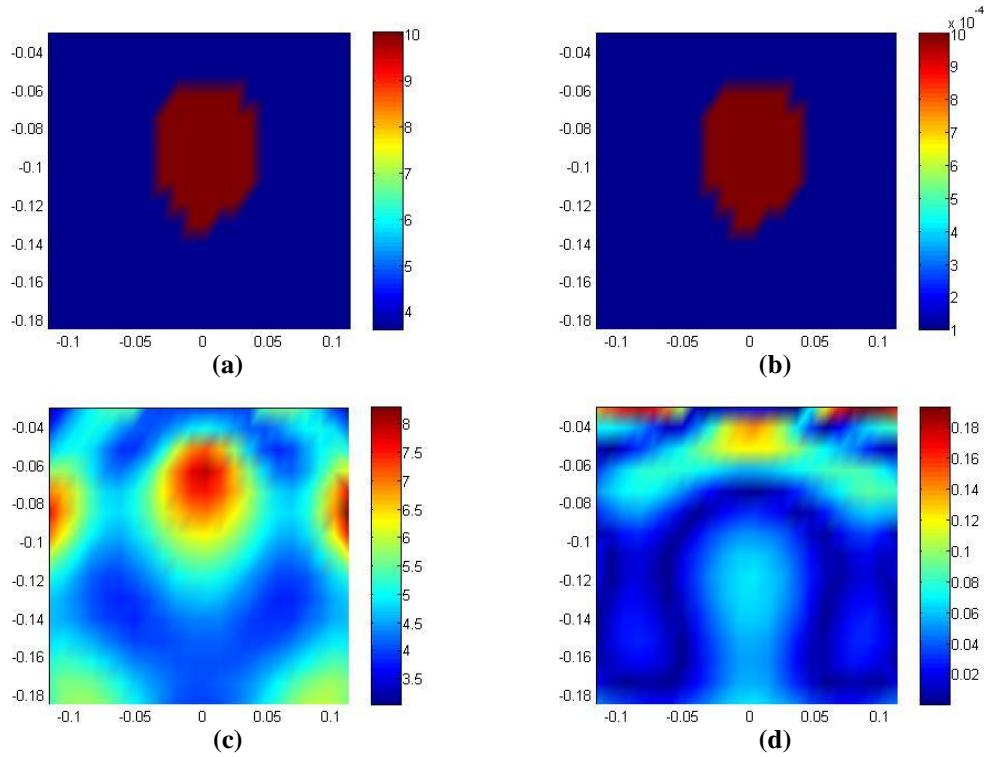
Figure 5.13:(a) Original relative dielectric permittivity **(b)**Original conductivity **(c)** Reconstructed relative dielectric permittivity **(d)** Reconstructed conductivity profile at $x_1=0$ for permittivity test for an object with $\varepsilon_{obj}=10\varepsilon_0$, $\sigma_{obj}=10^{-3}$.
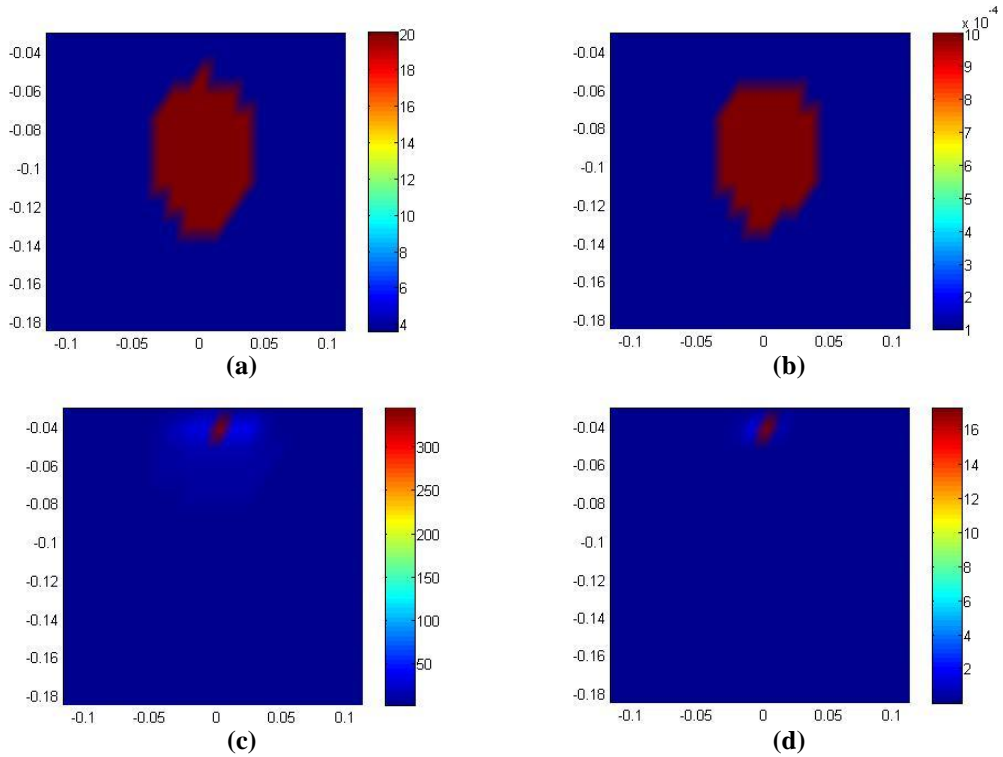
Figure 5.14:(a) Original relative dielectric permittivity **(b)**Original conductivity **(c)** Reconstructed relative dielectric permittivity **(d)** Reconstructed conductivity profile at $x_1=0$ for permittivity test for an object with $\varepsilon_{obj}=20\varepsilon_0$, $\sigma_{obj}=10^{-3}$.

When the difference between the dielectric permittivity of the object, which is $\varepsilon_{obj} = 20\varepsilon_0$ in the next example, and the one of the medium is higher, the reconstruction fails as shown in Figure 5.14. The values of both the permittivity and the conductivity of the object are extremely overestimated, and the shape of the object is not recognizable. However, it is still detected in both profiles, in Figure 5.14 (c) and (d).

Figures 5.12 – 14 show that the method successfully reconstructs the object within a certain amount of contrast range, and even when the contrast exceeds this range, the object can still be detected.

A contrast, within the range of successful reconstruction is tested for different medium and object parameters.An object with a dielectric permittivity $\varepsilon_{obj} = 10\varepsilon_0$ and a conductivity $\sigma_{obj} = 0.01$ is buried in a medium with parameters $\varepsilon_{obj} = 7\varepsilon_0$ and $\sigma_{obj} = 10^{-4}$. The reconstruction results in Figure 5.15 are consistent with previous reconstructions with similar contrast. The relative dielectric permittivity profile of the domain is successfully reconstructed in Figure 5.15 (c), with clear shape and location of the object, and the values are closely estimated. Similarly, the conductivity profile in Figure 5.15 (d) presents overestimated values, but provides with the location of the object, by showing the top of it.

The examples shown so far present the situation of the contrast when the parameters of the object are higher than the parameters of the medium. The next example is performed to test the contrast in a reversed situation. In this case, the object is assumed to be air, with free space parameters $\varepsilon_{obj} = \varepsilon_0$ and $\sigma_{obj} = 0$, and is buried in a medium with a dielectric permittivity $\varepsilon_{obj} = 3.6\varepsilon_0$ and a conductivity $\sigma_{obj} = 10^{-4}$. The simulation results of the example are shown in Figure 5.16. The reconstructed relative permittivity profile in Figure 5.16 (c) presents a good estimation of the objects shape and location, besides the values close to the real ones. Moreover, although the values in the conductivity profile are not in line with the real profile, the shape and location of the object are still clear.
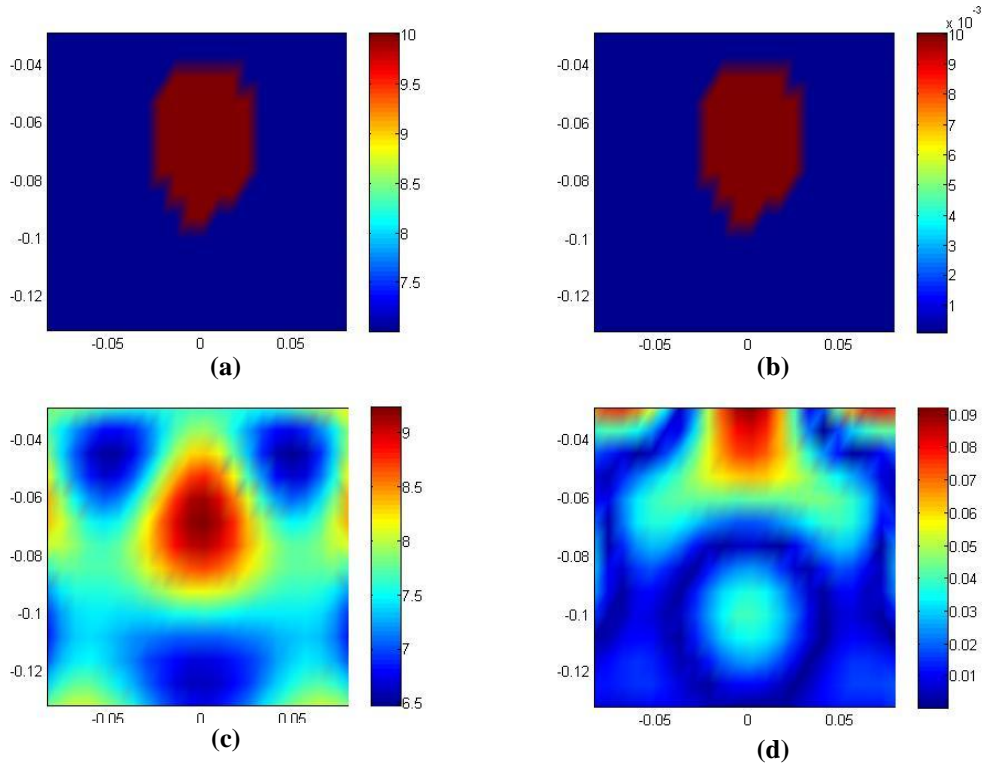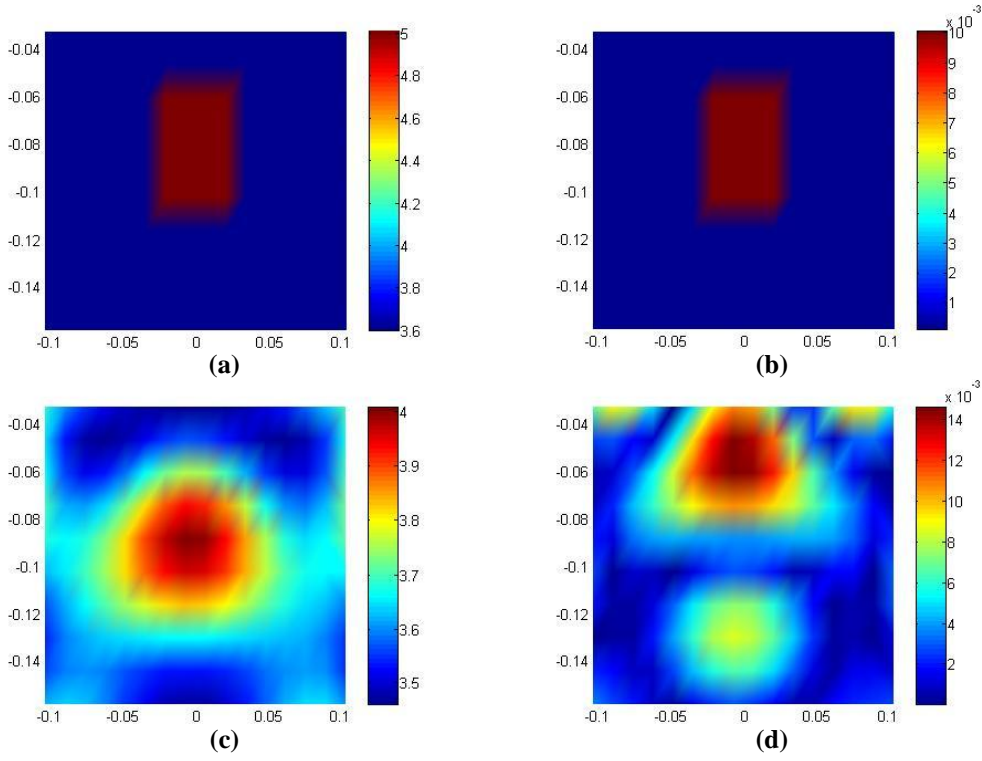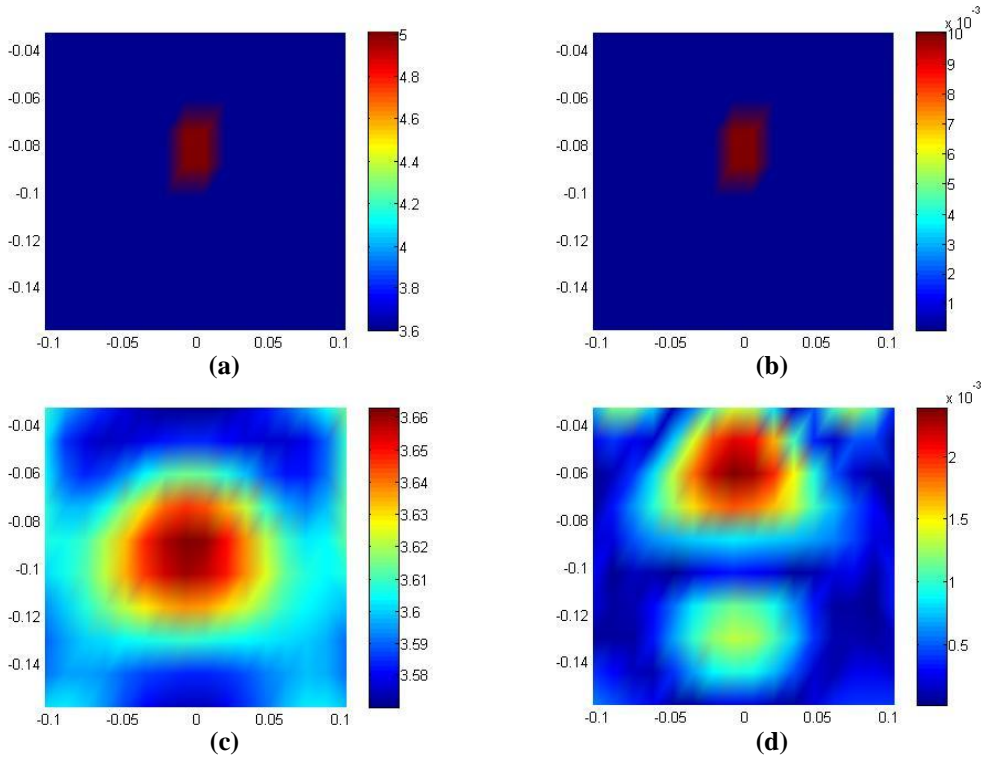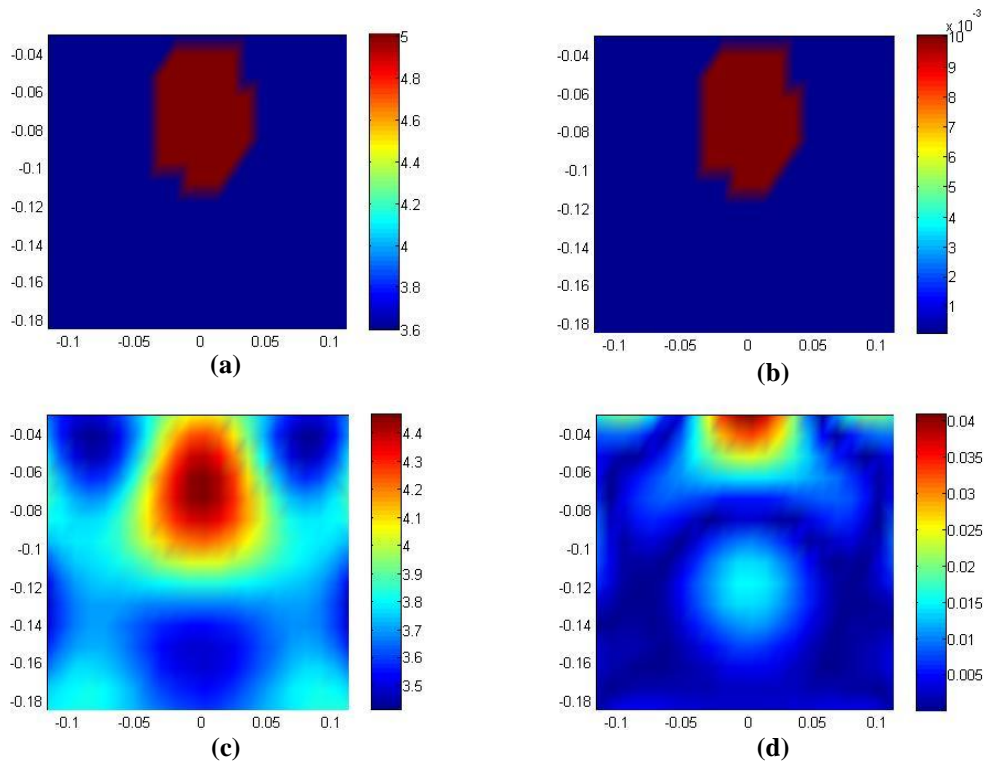
Figure 5.15:(a) Original relative dielectric permittivity **(b)**Original conductivity **(c)** Reconstructed relative dielectric permittivity **(d)** Reconstructed conductivity profile at $x_1=0$ for an object with $\varepsilon_{obj}=10\varepsilon_0$, $\sigma_{obj}=0.01$ that is buried in a medium with $\varepsilon_2=7\varepsilon_0$, $\sigma_2=10^{-4}$.
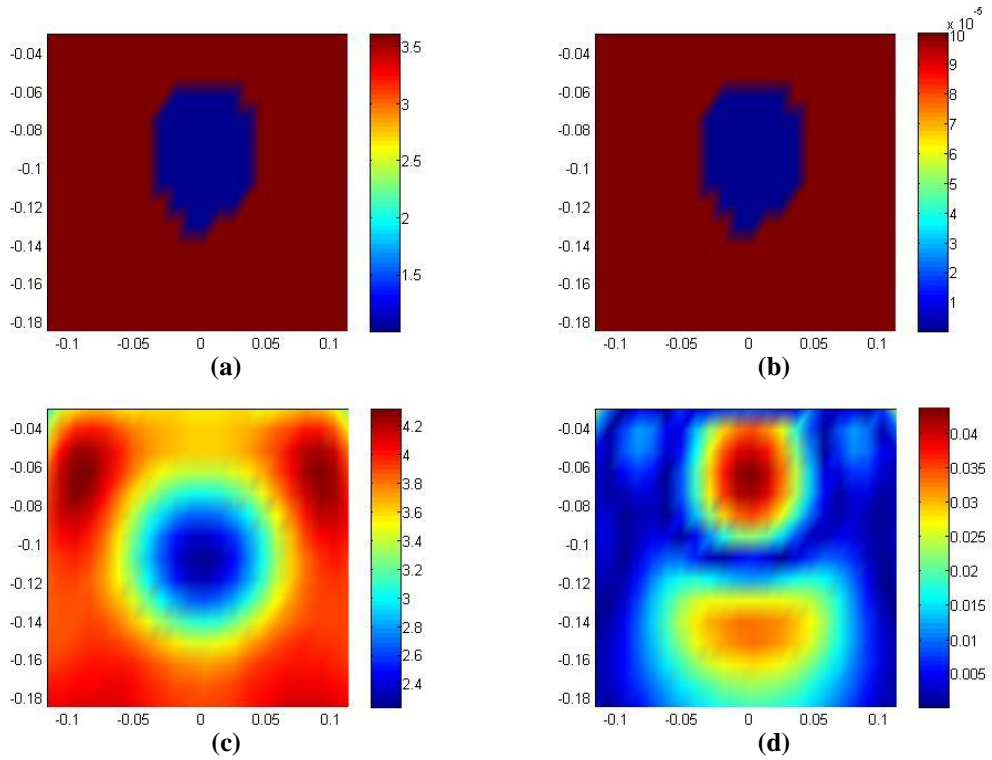
Figure 5.16:(a) Original relative dielectric permittivity **(b)**Original conductivity **(c)** Reconstructed relative dielectric permittivity **(d)** Reconstructed conductivity profile at $x_1=0$ for negative contrast test for an object with $\varepsilon_{obj}=\varepsilon_0$, $\sigma_{obj}=0$.

37

Figure 5.17:(a) Original relative dielectric permittivity **(b)**Original conductivity **(c)**Reconstructed relative dielectric permittivity **(d)** Reconstructed conductivity profile at $x_1=0$ for size test for a cubical object with a side length $0.2\lambda_{\text{soil}}$, and $\varepsilon_{\text{obj}}=5\varepsilon_0$, $\sigma_{\text{obj}}=0.01$.
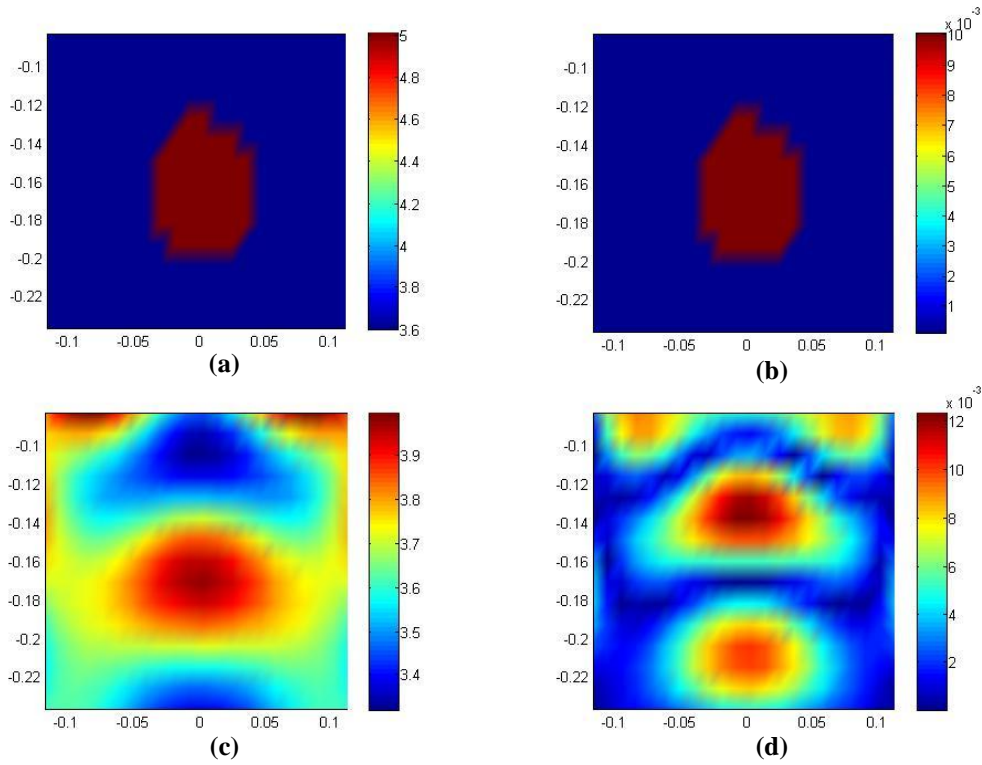

Figure 5.18:(a) Original relative dielectric permittivity **(b)**Original conductivity **(c)**Reconstructed relative dielectric permittivity **(d)** Reconstructed conductivity profile at $x_1=0$ for size test for a cubical object with a side length $0.1\lambda_{\text{soil}}$, and $\varepsilon_{\text{obj}}=5\varepsilon_0$, $\sigma_{\text{obj}}=0.01$.

Two cubical objects with $\varepsilon_{obj} = 5\varepsilon_0$ dielectric permittivity and $\sigma_{obj} = 0.1$ conductivity are centered at $\left(0,0,-0.3\lambda_{soil}\right)$, one with $0.2\lambda_{soil}$, and another $0.1\lambda_{soil}$ side length, whose simulation results can be seen in Figure 5.17 and Figure 5.18, respectively. Relative permittivity profiles in both figures present a good image of the object's shape and location, and its values are sufficiently estimated although the estimated value of the permittivity is closer to the real one for the bigger object. Similarly, both Figure 5.17 (d) and Figure 5.18 (d) present the location of the object by recovering its top, and the value appears closer to the real one for the bigger object, as expected.

The following three simulations are performed on objects buried at different depths under the rough surface. A spherical object, with $\varepsilon_{obj} = 5\varepsilon_0$ dielectric permittivity, $\sigma_{obj} = 0.01$ and a radius of $0.125\lambda_{soil}$ is centered at $\left(0,0,-0.275\lambda_{soil}\right)$, $0.05\lambda_{soil}$ below the lowest point of the rough interface. The simulation results in Figure 5.19 show a clear image of the object in the permittivity profile, as well as a close value for the permittivity. However, the conductivity profile presents the location of the object by showing the top of the object, and its value is overestimated.

Figure 5.19:(a) Original relative dielectric permittivity **(b)**Original conductivity **(c)** Reconstructed relative dielectric permittivity **(d)** Reconstructed conductivity profile at $x_1=0$ for depth test for an object buried $0.05\lambda_{soil}$ below the surface.
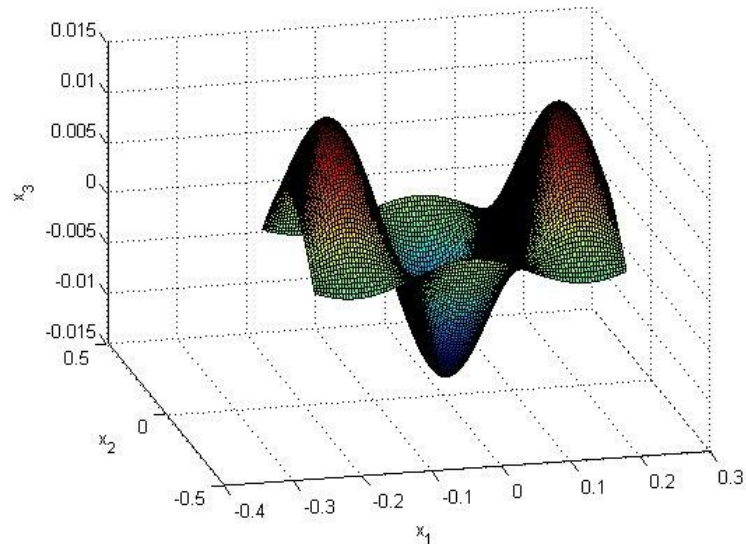
Figure 5.20:(a) Original relative dielectric permittivity **(b)**Original conductivity **(c)** Reconstructed relative dielectric permittivity **(d)** Reconstructed conductivity profile at $x_1=0$ for depth test for an object buried $0.5\lambda_{\text{soil}}$ below the surface.
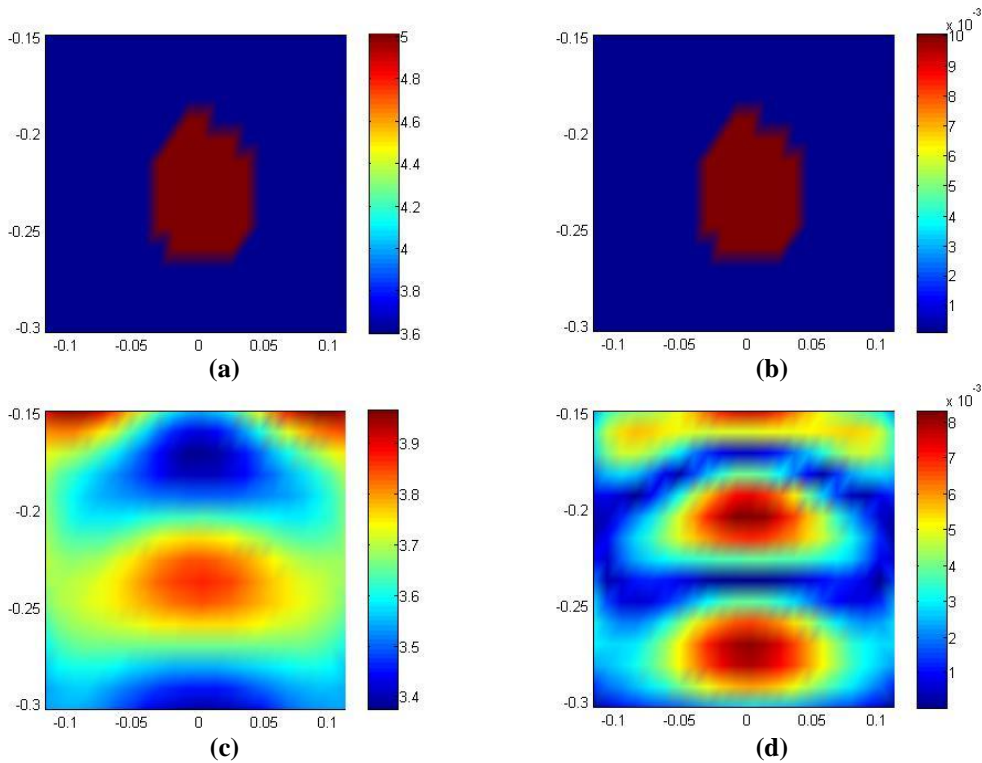
Figure 5.21:(a) Original relative dielectric permittivity **(b)**Original conductivity **(c)** Reconstructed relative dielectric permittivity **(d)** Reconstructed conductivity profile at $x_1=0$ for depth test for an object buried $0.75\lambda_{\text{soil}}$ below the surface.

Another object, with the same properties, is centered at $0, 0, -0.725\lambda_{soil}$, $0.5\lambda_{soil}$ below the lowest point of the rough interface. The values in Figure 5.20 (c) are slightly underestimated, and overestimated in Figure 5.20 (d). While the permittivity profile in (c) shows the shape and location of the object, although it is slightly misplaced, the conductivity profile in (d) shows its reflections, in addition to the object itself.

Another object with the same parameters is centered at an even deeper location, $0, 0, -0.975\lambda_{soil}$. The simulation results can be seen in Figure 5.21. The permittivity profile in Figure 21. (c) show a weaker image of the object, and reflections start to emerge, although its shape and location are still clear. However, the conductivity profile presents even higher values for the object's conductivity, and the reflections appear as strong as the object itself, making it impossible to distinguish the object from its reflections.

The following four simulations are run in order to observe the effect of the roughness's height. A spherical object with a radius $0.125\lambda_{soil}$ and constitutive parameters $\varepsilon_{obj} = 7$, and $\sigma_{obj} = 0.01$ is buried $0.05\lambda_{soil}$ below the lowest point of the roughness for each example. The medium was illuminated by 16 point sources, and the scattered field is obtained synthetically for 64 points on surfaces mentioned before. The reconstruction domain was divided into cubical cells with a side length $\lambda_{soil}/24$. For all four simulations, the same roughness profile is used, with different heights, which is defined as the difference between the highest and the lowest points of the surface.
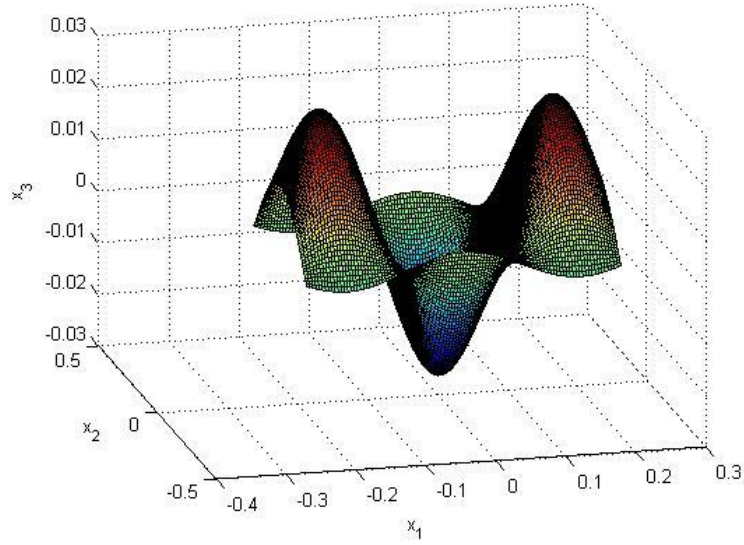
Figure 5.22: Surface profile with $0.1\lambda_{soil}$ height, which is used for the simulation shown in Figure 5.23.
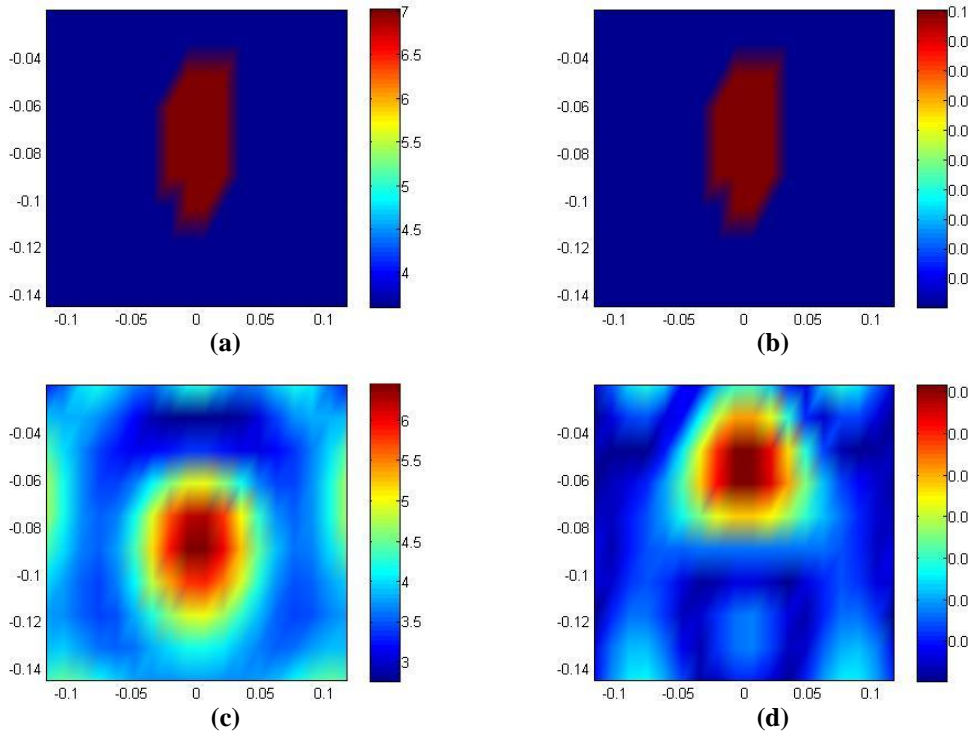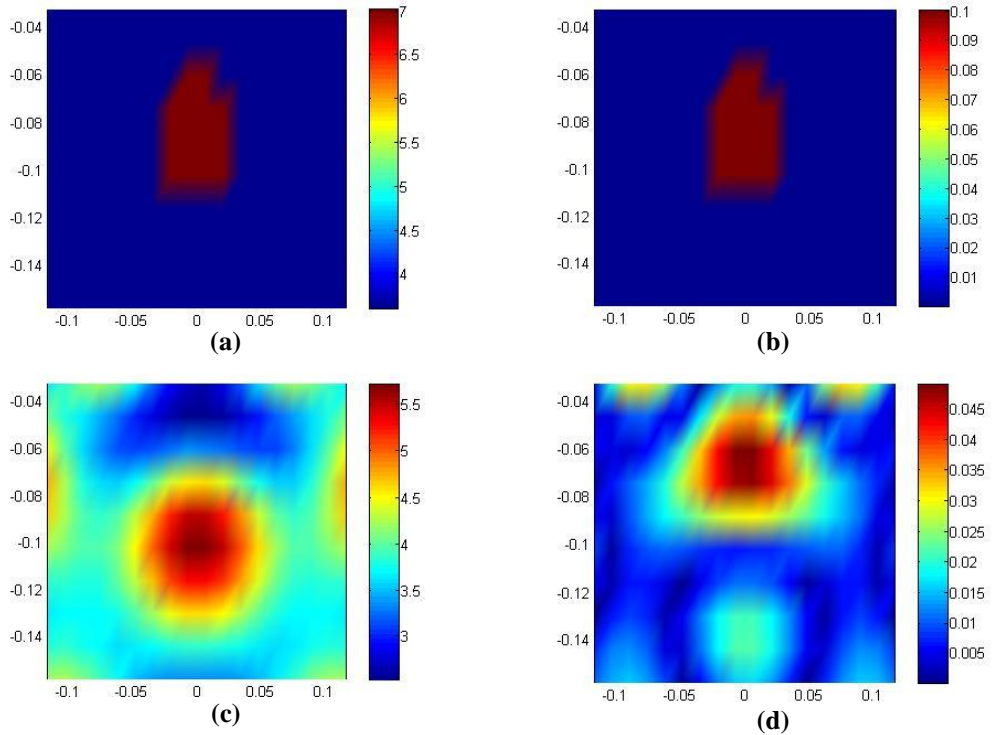

Figure 5.23:(a) Original relative dielectric permittivity **(b)** Original conductivity **(c)** Reconstructed relative dielectric permittivity **(d)** Reconstructed conductivity profile at $x_1=0$ for roughness height of $0.1\lambda_{soil}$.

The roughness with a height $0.1\lambda_{soil}$, which is shown in Figure 5.22, is used for the first example. The image of the reconstructed profile of relative dielectric permittivity in Figure 5.23 (c) show the object clearly but slightly mislocated, with a very good estimation of its value. Moreover, the conductivity profile in Figure 5.23 (d) show the location of the object, revealing only the top, and estimates the value roughly.

The roughness with a $0.2\lambda_{soil}$ height, which is used for the second example, can be seen in Figure 5.24. The simulation results in Figure 5.25 show that in the relative permittivity profile, the shape and location of the object is clear, yet slightly mislocated, its value is close to the real one, yet not as much as the one in the previous example. Expectedly, the conductivity profile, again, shows the top of the object, which reveals its location, and the value is roughly estimated.
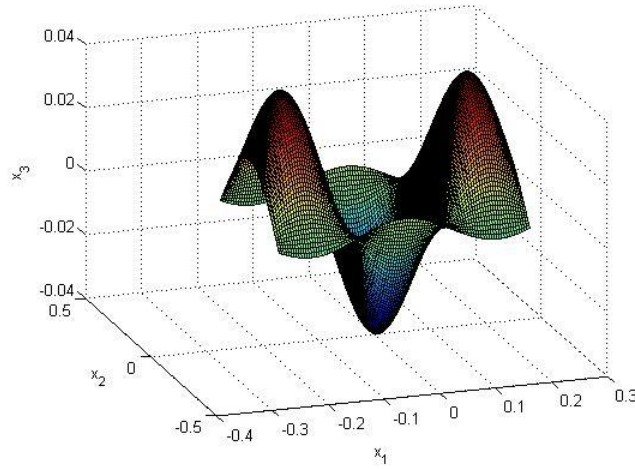
Figure 5.24: Surface profile with $0.2\lambda_{soil}$ height, which is used for the simulation shown in Figure 5.25.
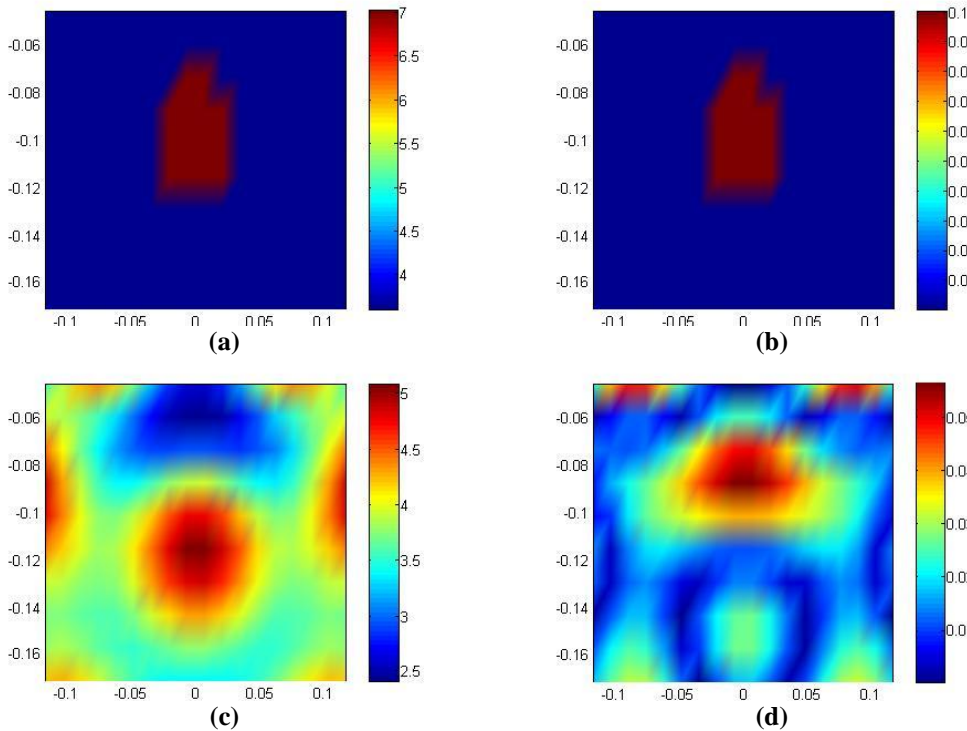

Figure 5.25:(a) Original relative dielectric permittivity **(b)**Original conductivity **(c)** Reconstructed relative dielectric permittivity **(d)** Reconstructed conductivity profile at $x_1=0$ for roughness height of $0.2\lambda_{soil}$.

The third example is performed using the rough surface shown in Figure 5.26, which is $0.3\lambda_{soil}$ high, and its results can be seen in Figure 5.27. The reconstructed relative permittivity and conductivity profiles in Figure 5.27 (c) and (d), respectively, support the results in the previous examples. The object itself is clear in (c) and its top in (d).

The values are still close to the real ones, but the estimation is weaker, due to the increase in the height of the roughness, which is expected.

Figure 5.26: Surface profile with $0.3\lambda_{soil}$ height, which is used for the simulation shown in Figure 5.27.

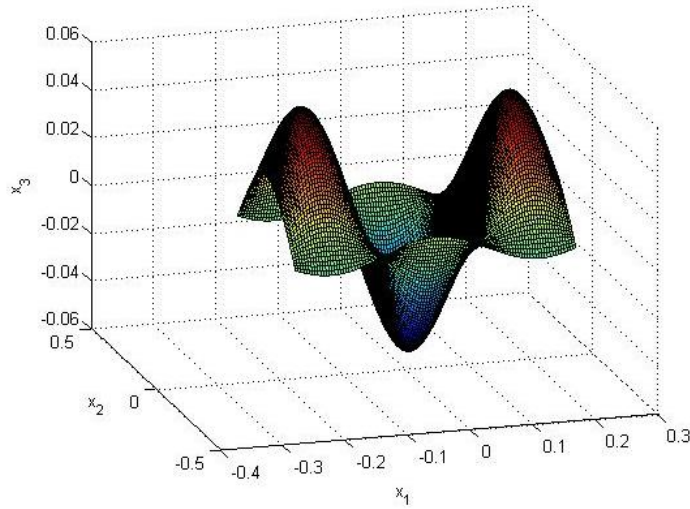**Figure 5.27:(a)**Original relative dielectric permittivity **(b)**Original conductivity **(c)** Reconstructed relative dielectric permittivity **(d)** Reconstructed conductivity profile at $x_1=0$ for roughness height of $0.3\lambda_{soil}$.

The simulation results of the fourth example, which is done using the roughness with a height of $0.4\lambda_{soil}$ in Figure 2.28, can be seen in Figure 2.29. Although the shape and location of the object are revealed as expected in both profiles in (c) and (d), and the estimated values in these profiles are less close to the real values, they do not seem to

be very different from the previous example. It suggests that the nonlinearity the rough surface brings to the problem does not increase linearly, which means while the change in smaller values of its height has more visible effects on the reconstruction than the same change in larger values.


Figure 5.28: Surface profile with $0.4\lambda_{soil}$ height, which is used for the simulation shown in Figure 5.29.
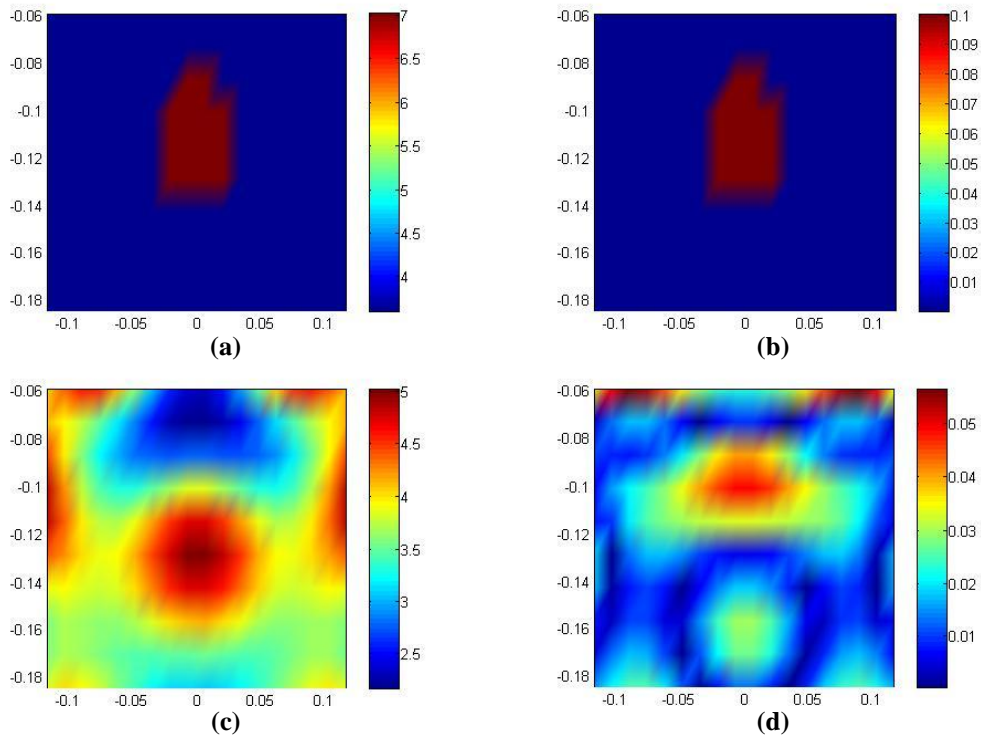
Figure 5.29:(a) Original relative dielectric permittivity **(b)**Original conductivity **(c)** Reconstructed relative dielectric permittivity **(d)** Reconstructed conductivity profile at $x_1=0$ for roughness height of $0.4\lambda_{soil}$.

In the following examples, a more challenging situation, the situation that involves two objects is investigated. Two identical spherical objects with a relative dielectric permittivity $\varepsilon_{obj} = 7$, conductivity $\sigma_{obj} = 0.2$, and a radius $0.05\lambda_{soil}$ are placed $0.05\lambda_{soil}$ below the lowest point of the $0.15\lambda_{soil}$ high rough surface shown in Figure 5.30. The medium was illuminated by 25 point sources, and the scattered field was obtained synthetically at 81 measurement points. The reconstruction domain was divided into cubical cells with side length $\lambda_{soil}/18$.
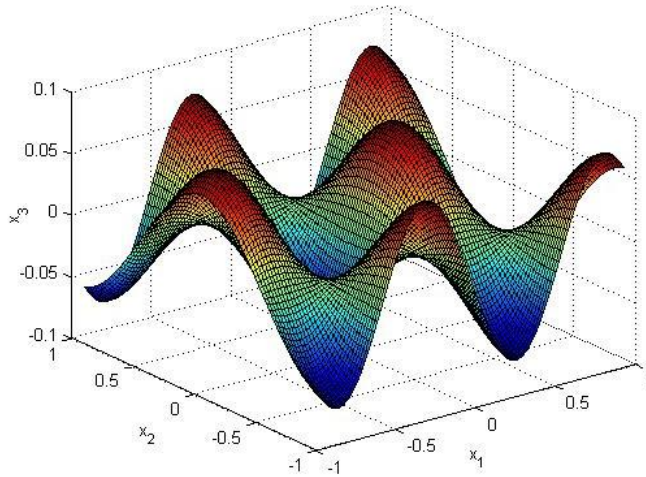

Figure 5.30: Surface profile used for the next three simulations, shown through Figure 5.31-5.33.

Figure 5.31 shows the simulation results of the case when the two objects mentioned are placed $0.75\lambda_{soil}$ apart from each other. The relative permittivity profile in Figure 5.31 (b) shows a close estimation of the value, and the shape and location of the objects explicitly, although some mislocation and reflections are also observed, due to the high conductivity of the object. On the other hand, although the values of conductivity in Figure 5.31 (d) are not sufficiently estimated and reflections are present, the location of the objects are very clear.

The same objects are placed closer, $0.5\lambda_{soil}$ apart from each other for the next example. The simulation results in Figure 5.32 are very similar to the ones in the previous example. The estimated values of both relative permittivity and conductivity profiles are almost the same, both objects are clearly visible, and reflections are observed, as in the previous example. However, the objects in the permittivity profile appear to be beginning to merge with each other, which suggests that the $0.5\lambda_{soil}$ distance between them is the lower limit to distinguish them separately.
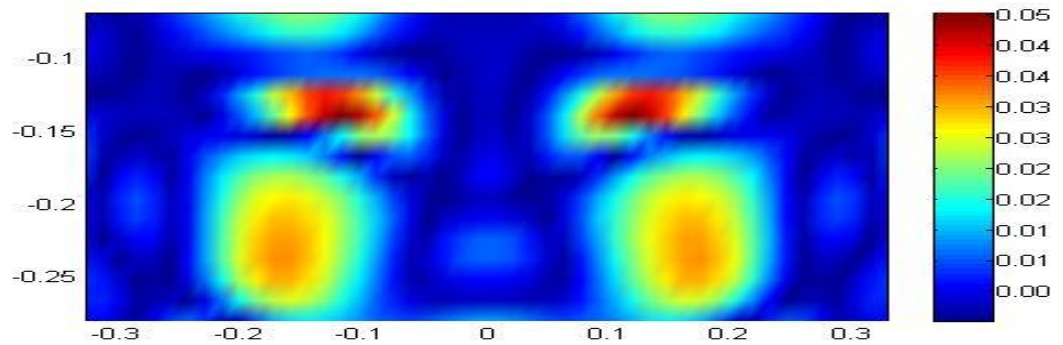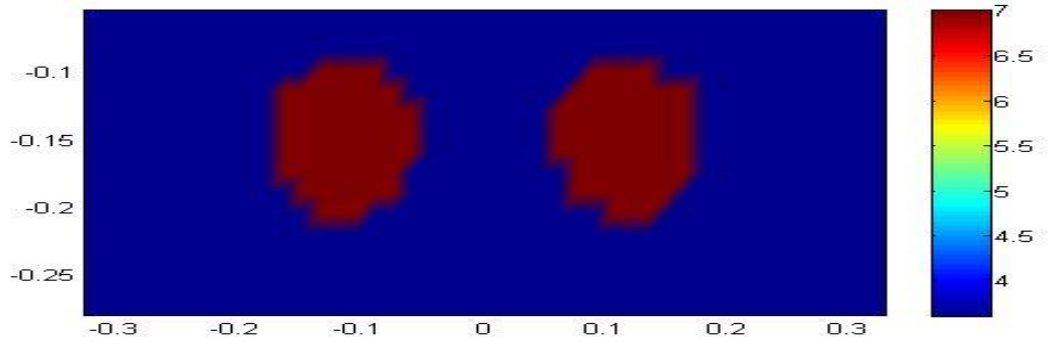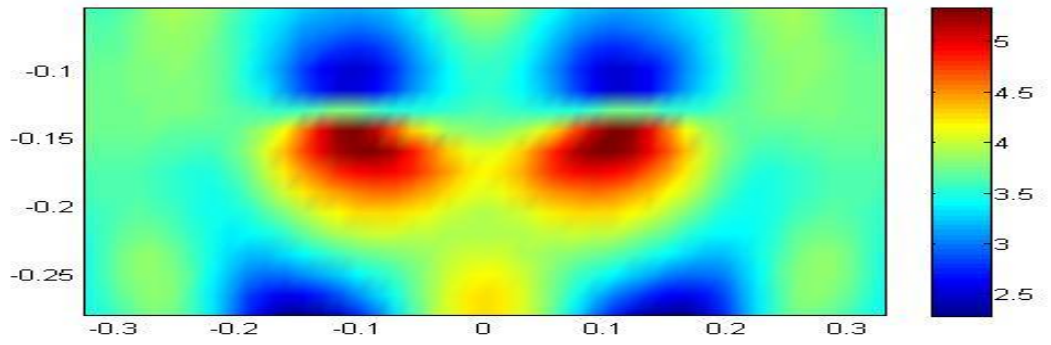
46
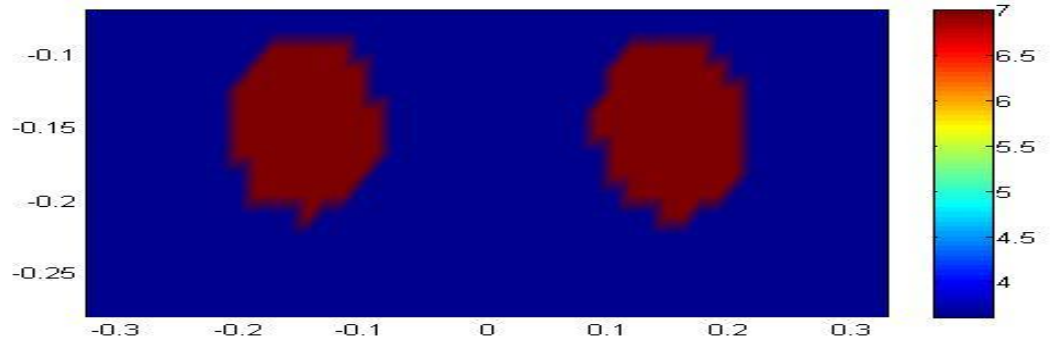
(a)
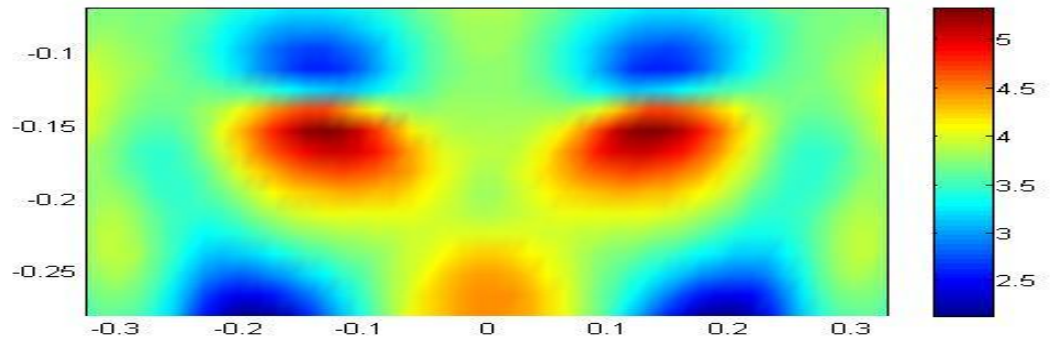
(b)
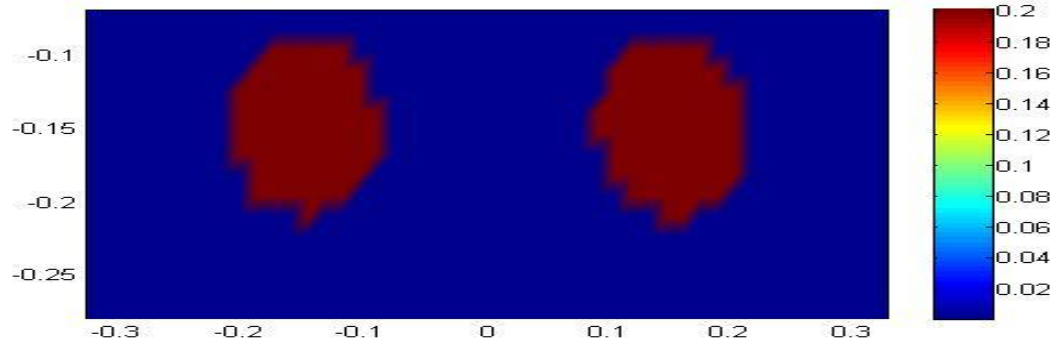
(c)

(d)

Figure 5.31:(a) Original relative dielectric permittivity **(b)**Reconstructed relative dielectric permittivity**(c)**Original conductivity **(d)** Reconstructed conductivity profile at x_1=0 for resolution test for two spherical objects withε_{obj}=7ε_0, σ_{obj}=0.2, lying 0.75λ_{soil} apart from each other.

(a)

(b)

(c)

(d)

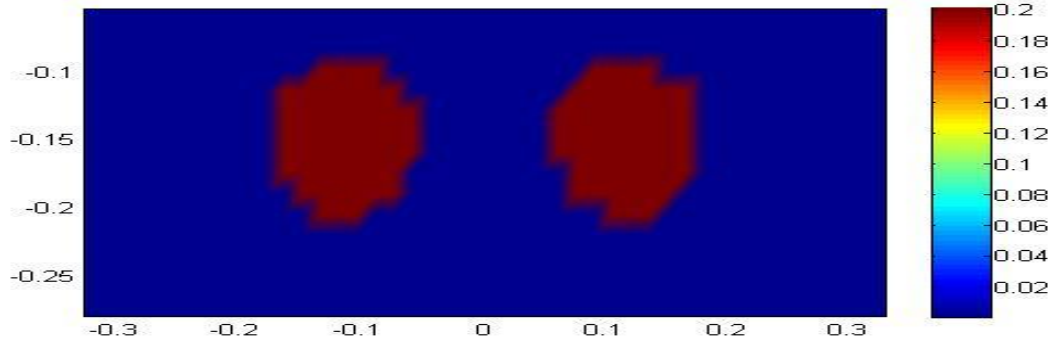**Figure 5.32:(a)**Original relative dielectric permittivity **(b)**Reconstructed relative dielectric permittivity**(c)**Original conductivity **(d)** Reconstructed conductivity profile at $x_1=0$ for resolution test for two spherical objects with$\varepsilon_{obj}=7\varepsilon_0$, $\sigma_{obj}=0.2$, lying $0.5\lambda_{soil}$ apart from each other.
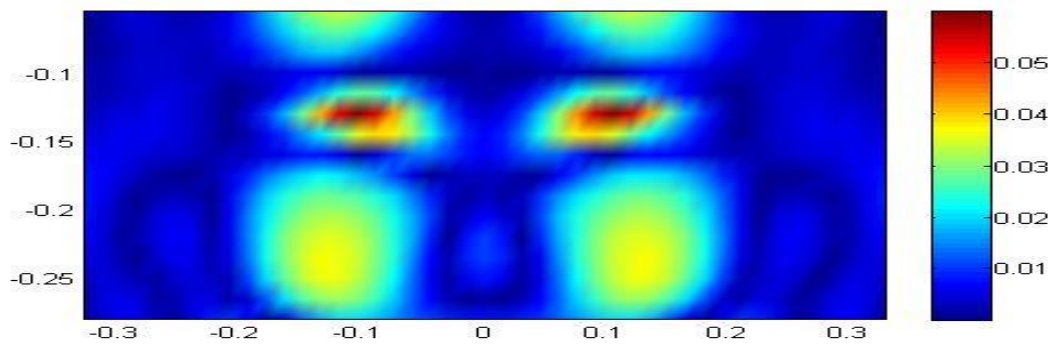
48

(a)

(b)

(c)

(d)

Figure 5.33:(a) Original relative dielectric permittivity **(b)**Reconstructed relative dielectric permittivity **(c)**Original conductivity **(d)** Reconstructed conductivity profile at $x_1=0$ for resolution test for two spherical objects with$\varepsilon_{obj}=7\varepsilon_0$, $\sigma_{obj}=0.2$, lying $0.2\lambda_{soil}$ apart from each other.
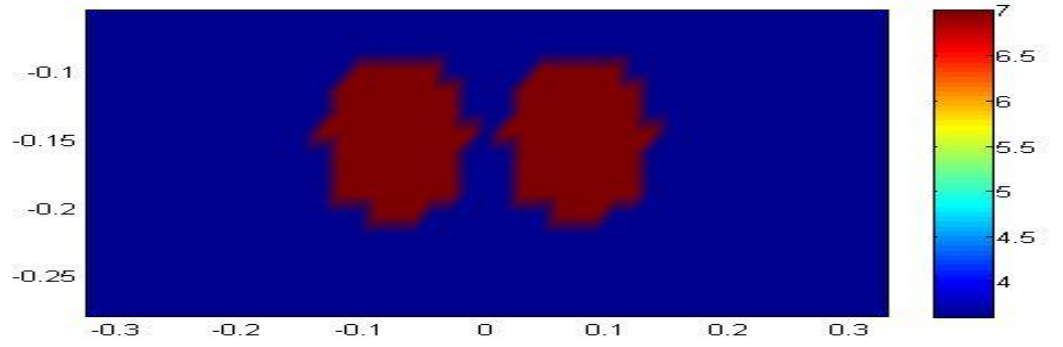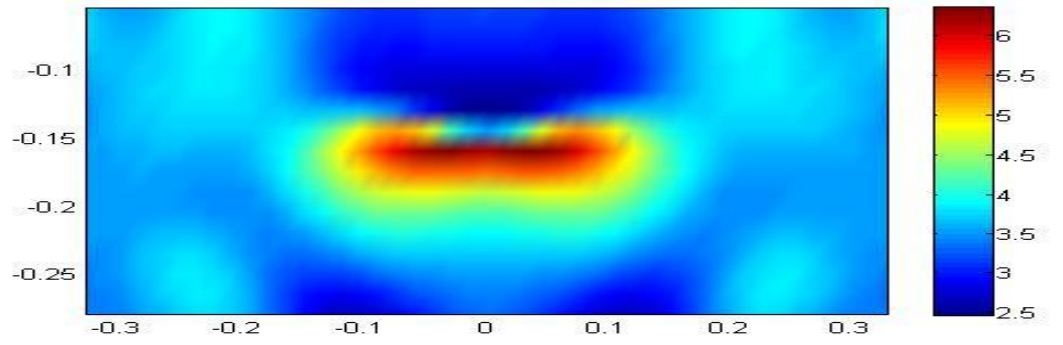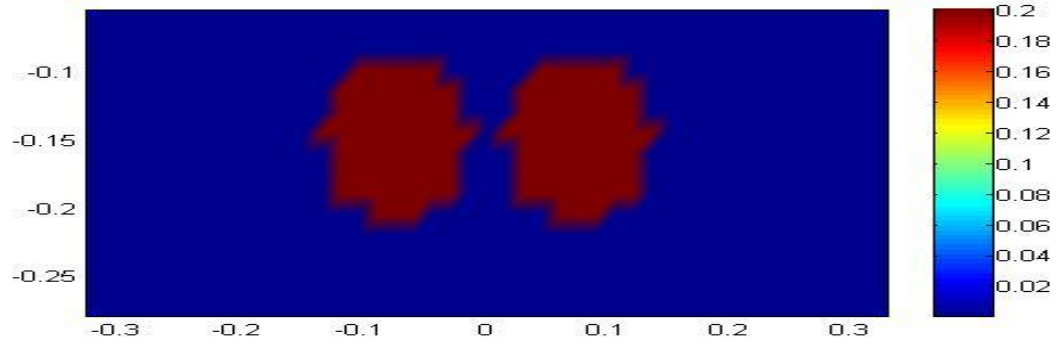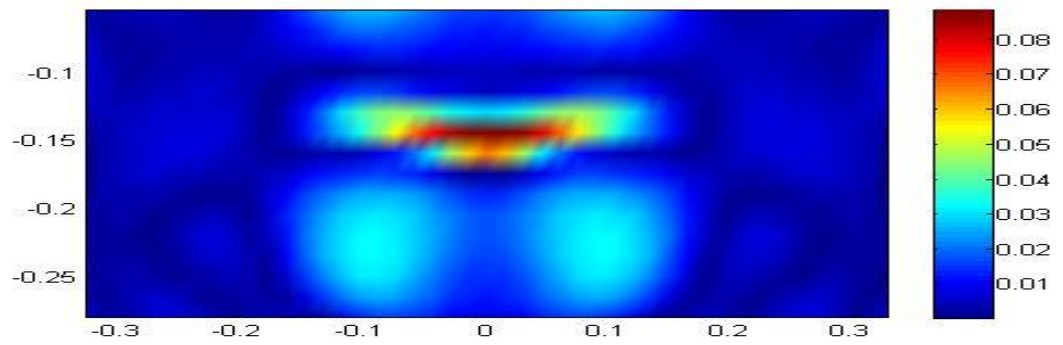
In order to test this, and investigate further what happens when the two objects are even closer, another simulation, in which they are placed $0.2\lambda_{soil}$ apart from each other, is performed. The results of the simulation, which are shown in Figure 5.33, show that the two objects are no longer visible as separate objects, but they appear to be one bigger object, whose location is clear in both relative permittivity and conductivity profiles, having weaker reflections than before. Moreover, although the estimated value of the object's conductivity is still insufficient, values in both profiles are now closer to the real one, which supports findings in earlier examples that the estimations are more accurate for bigger objects.
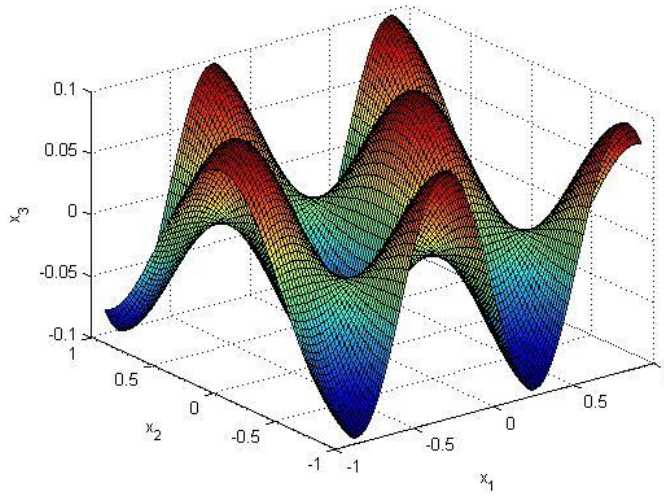
Figure 5.34: Surface profile used for the next simulation, shown through in Figure 5.35.

Another example is performed for two objects having different constitutive parameters. Two spherical objects with a $0.05\lambda_{soil}$ radius, one with constitutive parameters $\varepsilon_{obj1} = 5$, $\sigma_{obj1} = 0.1$, and the other $\varepsilon_{obj2} = 7$, $\sigma_{obj2} = 0.2$ are located $0.75\lambda_{soil}$ apart from each other, and $0.05\lambda_{soil}$ below the lowest point of the rough surface, which is $0.2\lambda_{soil}$ high, and shown in Figure 5.34. The medium is illuminated by 36 sources, and the scattered field is evaluated for 121 points, and the reconstruction domain is divided into cubical cells with side length $\lambda_{soil}/16$. The conductivity profile in Figure 5.35 (d) fails to estimate the values while it still shows where the objects are located in spite of the reflections. However, the relative permittivity profile in Figure 5.35 (b), although reflections are present, shows the shape and location of the objects, and a close estimation of the values.
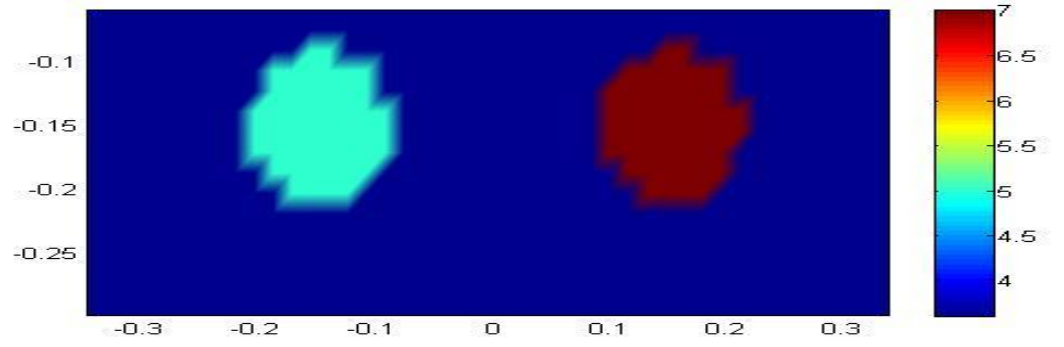
(a)
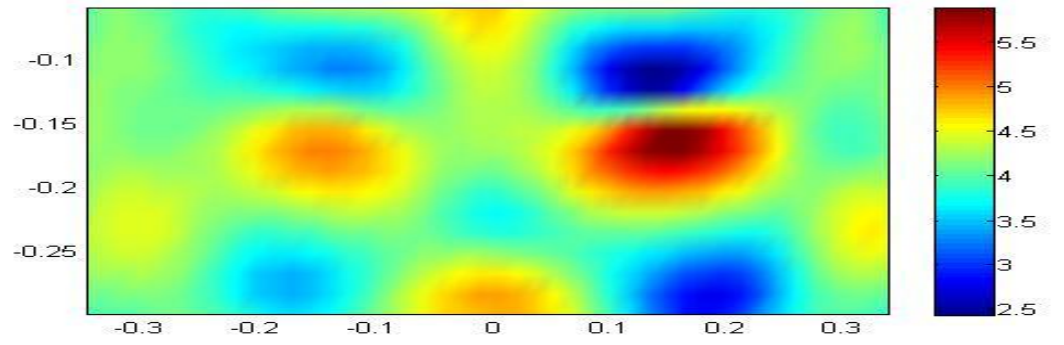
(b)
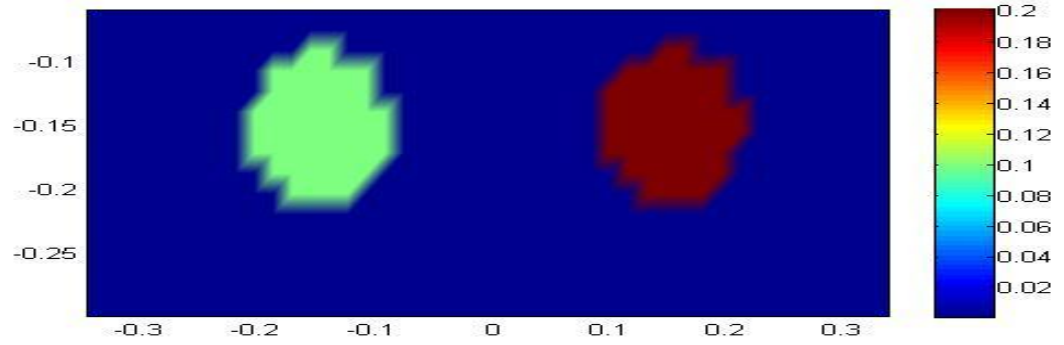
(c)

(d)

Figure 5.35:(a) Original relative dielectric permittivity **(b)**Reconstructed relative dielectric permittivity **(c)**Original conductivity **(d)** Reconstructed conductivity profile at $x_1=0$ for two spherical objects with$\varepsilon_{obj1}=5\varepsilon_0$, $\sigma_{obj1}=0.1$, and $\varepsilon_{obj2}=7\varepsilon_0$, $\sigma_{obj2}=0.2$, lying $0.75\lambda_{soil}$ apart from each other.

For the last example in this section, the $0.2\lambda_{soil}$ high rough surface shown in Figure 5.36, and two identical objects in the shape of rectangular prism with side lengths $0.2\lambda_{soil} \times 0.2\lambda_{soil} \times 0.4\lambda_{soil}$, and constitutive parameters $\varepsilon_{obj} = 7$ and $\sigma_{obj} = 0.01$, are used. One object was placed horizontally, and the other vertically, $0.75\lambda_{soil}$ apart from each other, and $0.05\lambda_{soil}$ below the lowest point of the rough surface. 25 illuminations and 81 measurement points were used, and the reconstruction domain was divided into cubical cells with side length $\lambda_{soil}/21$. The relative permittivity profile in Figure 5.37 (b) shows the location of the objects clearly. Although the shape is not as clear as desired, it still gives an idea. It also gives an acceptable, but insufficient estimation of the values. On the other hand, the conductivity profile gives only an approximate location of the objects, and it fails to present the shape and an acceptible estimate of the values.

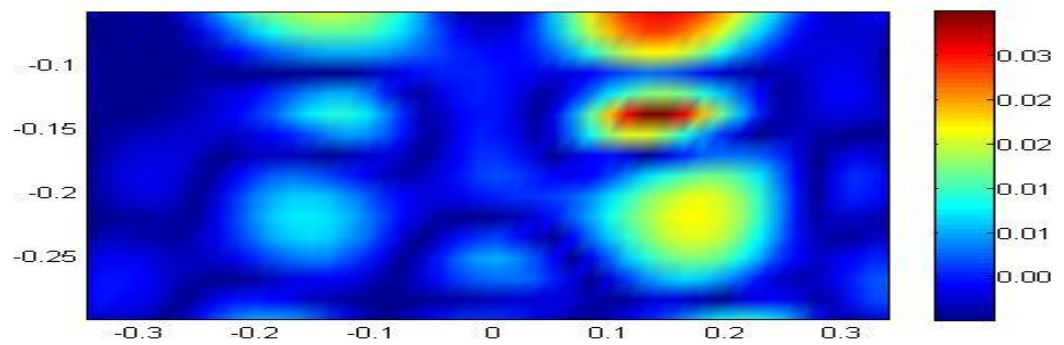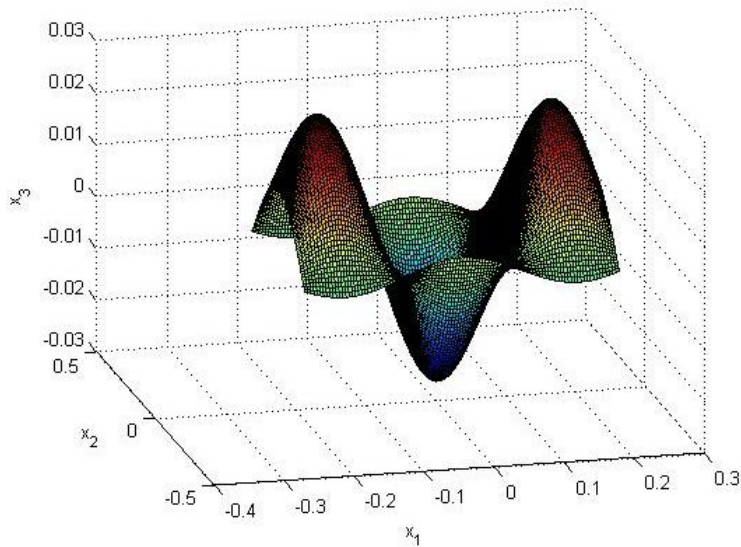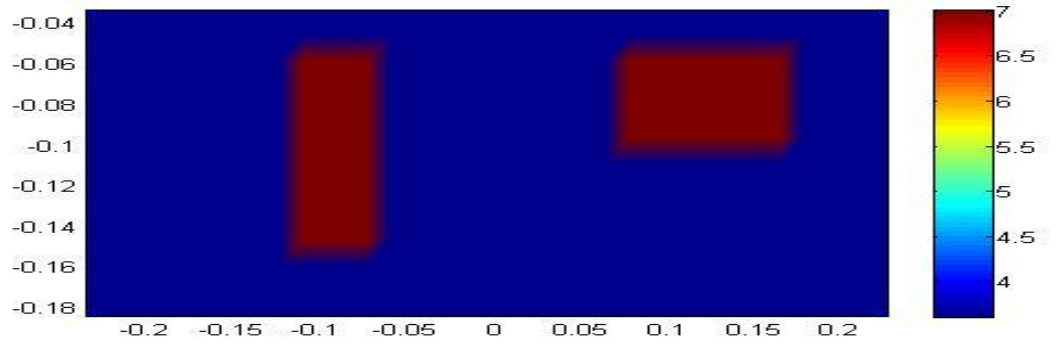**Figure 5.36:**Surface profile used for the last simulation, shown in Figure 5.37.
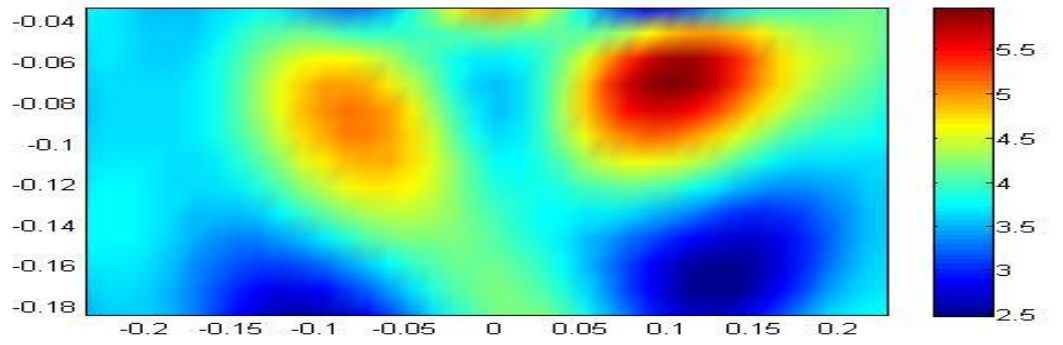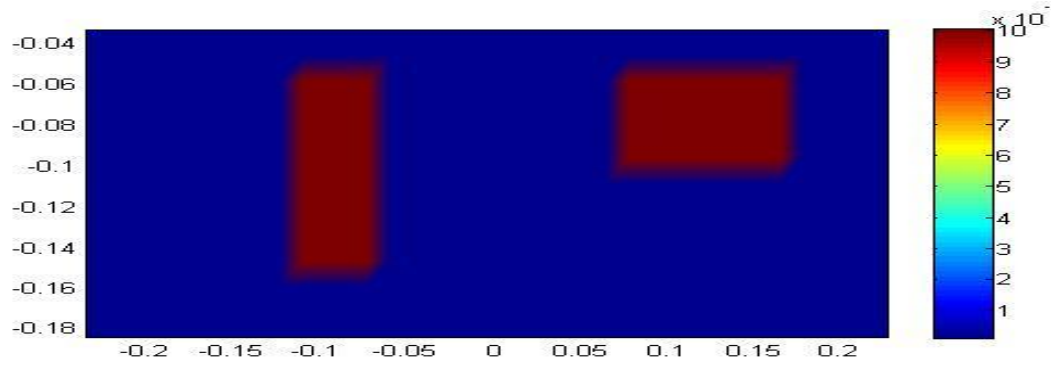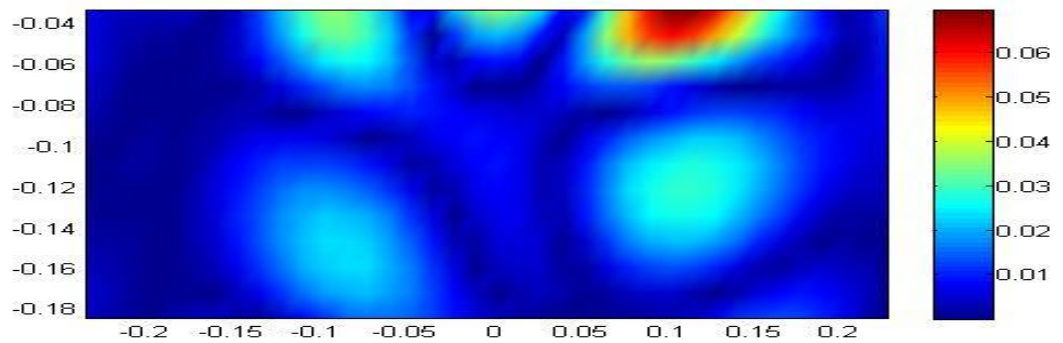
Figure 5.37:(a) Original relative dielectric permittivity **(b)**Reconstructed relative dielectric permittivity**(c)**Original conductivity **(d)** Reconstructed conductivity profile at x_1=0 for two objects in the shape of a rectangular prism with $0.2\lambda_{soil} \times 0.2\lambda_{soil} \times 0.4\lambda_{soil}$ size, andε_{obj}=7ε_0, σ_{obj}=0.01.

6. CONCLUSIONS

A nonlinear tomographic approach for a 3D scalar case of microwave imaging of dielectric objects buried under a rough surface is presented. The contribution of the rough surface to the background of the object is obtained via the Buried Object Approach (BOA), which involves obtaining the Green's function of the two half-spaces with a planar interface, and then treating the roughness as a series of objects embedded in both half-spaces alternately. The resulting system of integral equations is solved for the contrast function via Contrast Source Inversion (CSI) method.

The efficiency of the medhod has been tested through numerical simulations with noise added data, and despite the physical obstacles of the subsurface imaging such as limited illumination and measurement, it has been shown that the approach yields good reconstructions. The method has proven to be effective in a large band of frequencies. Different sets of constitutive parameters for both the object and the medium it lies within have been tested, and the values have been very well reconstructed. In fact, even the objects with higher constitutive parameters were detected, if not clearly reconstructed. The method has also proven to successfully detect and reconstruct objects with a significantly small size. It has been observed that the geometry of the roughness does not considerably affect the quality of the reconstuctions. However, although sufficient results have been obtained even for considerably high roughnesses and objects that are buried relatively deep, the reconstuctions have been more satisfactory for shallow objects buried under slight roughnesses. In the cases when multiple objects are involved, as long as they are at least half the wavelength of the medium apart from each other, even if they have different constitutive parameters or shapes, they have been clearly distinguished and effectively reconstructed.It should be noted that a priori information about the positivity of the contrast has been applied in order to enhance the performance of the method. However, it has been shown that even an object with negative contrast values, such as one whose constitutive parameters are equal to those of air buried into dry soil, has been successfully reconstructed without applying any a priori

information during the inversion procedure. Therefore, the simulations show that the proposed method is applicable for imaging of buried dielectric objects under rough surface, but also detection and determination of pipesor tunnels.

Further studies are planned to extend the proposed approach to 3Dvectoral case of imaging dielectric objects buried under a rough surface for more realistic applications, and to employ computation algorithms in order to overcome the computational complexity and time.

REFERENCES

[1] **Kouali, M., Kubické, G., & Bourlier, C.**(2012). Extended Propagation-Inside-Layer Expansion Method Combined with the Forward-Backward Method to Study the Scattering from an Object Above a Rough Surface.*OPTIC LETTERS,37*, 2985-2987.

[2] **Bourlier, C., Kubické, G., & Déchamps, N.**(2008). Fast Method to Compute Scattering by a Buried Object Under a Randomly Rough Surface: PILE Combined with FB-SA, *Opt. Soc. Am. A,25*, 891-902.

[3] **Lin, Z.-W., Xu X., Zhang, X.-J., & FANG, G.-Y.**(2011). Electromagnetic Scattering and Inverse Scattering of Layered Media with a Slightly Rough Surface, *Chin. Phys. Lett., 28*,1-4.

[4] **Cmielewski, O., Saillard, M., Belkebir, K., & Tortel,H.**(2006). On the Characterization of Buried Targets Under a Rough Surface Using the Wigner-Ville Transformation, *IEEE Geoscience and Remote Sensing Letters,3*, 442-446.

[5] **Cmielewski, O., Tortel, H., Litman, A., & Saillard, M.**(2007). A Two-Step Procedure for Characterizing Obstacles Under a Rough Surface From Bistatic Measurements, *IEEE Transactions on Geoscience and Remote Sensing, 45*, 2850-2858.

[6]**O'Neill, K.**(2000). Broadband Bistatic Coherent and Incoherent Detection of Buried Objects Beneath Randomly Rough Surfaces, *IEEE Transactions on Geoscience and Remote Sensing, 38*, 891-898.

[7] **Cmielewski, O., Saillard, M., & Tortel, H.**(2007). Detection of Buried Objects Beneath a Rough Surface, *Waves in Random and Complex Media,16*, 417-431.

[8] **Bo, L., Dabbiru, S., Anh, H. T., & Chung, P.**(2006). Surface and Buried Mine Detection Using MWIR Images, *Proceedings of SPIE,6217*, 1-12

[9] **El-Shenawee, M.**(2003). Remote Sensing of Penetrable Objects Buried Beneath Two-Dimensional Random Rough Surfaces by Use of the Mueller Matrix Elements, *Journal of Opt. Soc. Am. A., 20*, 183-194.

[10]**El-Shenawee, M.**(2004). Polarimetric Scattering From Two-Layered Two-Dimensional Random Rough Surfaces With and Without Buried Objects, *IEEE Transactions on Geoscience and Remote Sensing, 42*, 67-76.

[11] **Li, F., Chen, X., & Huang, K.**(2008).Microwave Imaging of Buried Object by the GA and Using the s_{11}Parameter, *Progress In Electromagnetic Research, PIER,85,* 289-302.

[12]**Chen, X., & Huang, K.**(2005).Microwave Imaging of Buried Inhomogeneous Objects Using Parallel Genetic Algorithm Combined with FDTD Method,*Progress In Electromagnetics Research, PIER, 53*, 283-298.

[13] **Caorsi, S., Massa, A., Pastorino, M., Raffetto, M., & Randazzo, A.**(2003). Detection of Buried Inhomogeneous Elliptic Cylinders by a Memetic Algorithm, *IEEE Transactions on Antennas and Propagation, 51*, 2878-2884.

[14] **Şahintürk, H., Yapar, A., & Akduman, I.**(2004). On the Use of Surface Impedance in the Detection and Location of Buried Objects, *International Journal of Electronics and Communications, 58*, 249-255.

[15] **Altuncu, Y., Akduman, I., & Yapar, A.**(2007). Detecting and Locating Dielectric Objects Buried Under a Rough Interface, *IEEE Geoscience and Remote Sensing Letters, 4*, 251-255.

[16] **Morrow, I., & Genderen, P. V.**(2002). Effective Imaging of Buried Dielectric Objects, *IEEE Transactions on Geoscience and Remote Sensing, 40*, 943-949.

[17] **Wang, Y., Longstaff, I. D., & Leat, C. J.**(2001). SAR Imaging of Buried Objects from MoM Modelled Scattered Field, *IEE Proceedings Radar, Sonar and Navigation, 148*, 167-172.

[18] **Cakoni, F., Fares, M., & Haddar, H.**(2006). Analysis of Two Linear Sampling Methods Applied to Electromagnetic Imaging of Buried Objects, *Inverse Problems, 22*, 845-867.

[19] **Ozdemir, O., & Haddar, H.**(2010). Preprocessing the Reciprocity Gap Sampling Method in Buried-Object Imaging Experiments, *IEEE Geoscience and Remote Sensing Letters, 7*, 756-760.

[20] **Dubois, A., Belkebir, K., & Saillard, M.**(2004). Localization and Characterization of Two-Dimensional Targets Buried in a Cluttered Environment, *Inverse Problems,20*, 63-79.

[21] **Zhu, X., Zhao, Z., Yang, W., Zhang, Y., Nie, Z.-P., & Liu, Q. H.**(2011). Iterative Time-Reversal Mirror Method for Imaging the Buried Object Beneath Rough Ground Surface, *Progress in Electromagnetics Research,117*, 19-33.

[22] **Firoozabaldi, R., Miller, E. L., Rappaport, C.M., & Morgenthaler, A.W.**(2005). New Inverse Method for Simultaneous Reconstruction of Object Buried Beneath Rough Ground and the Ground Surface Structure Using SAMM Forward Model, *Proceedings of SPIE-IS&T Electronic Imaging, SPIE, 5674*, 382-393.

[23] **Firoozabaldi, R., Miller, E. L., Rappaport, C. M., & Morgenthaler, A. W.**(2007). Subsurface Sensing of Buried Objects Under a Randomly Rough Surface Using Scattered Electromagnetic Field Data, *IEEE Transactions on Geoscience and Remote Sensing, 45*, 104-117.

[24] **Lambert, M., Lesselier, D., & Kooij, B. J.**(1998). The Retrieval of a Buried Cylindrical Obstacle by a Constrained Modified Gradient Method in

the H Polarization Case and for Maxwellian Materials, *Inverse Problems,14*, 1265-1283.

[25] **Vertiy, A. A., & Gavrilov, S. P.**(1998). Modeling of Microwave Images of Buried Cylindrical Objects, *International Journal of Infrared and Millimeter Waves,19*, 1201-1220.

[26] **Cui, T. J., Aydiner, A. A., Chew, W. C., Wright, D. L., & Smith, D. V.**(2003). Three-Dimensional Imaging of Buried Objects in Very Lossy Earth by Inversion of VETEM Data, *IEEE Transactions on Antennas and Propagation,41*, 2197-2210.

[27] **Chaturverdi, P., & Plumb, R. G.**(1995). Electromagnetic Imaging of Underground Targets Using Constrained Optimization, *IEEE Transactions on Geoscience and Remote Sensing,33*, 551-561.

[28] **Yu, Y., Yu, T., & Carin, L.**(2004). Three Dimensional Inverse Scattering of a Dielectric Target Embedded in a Lossy Half-Space, *IEEE Transactions on Geoscience and Remote Sensing,42*, 957-973.

[29] **Cui, T. J., Qin, Y., Ye, Y., Wu, J., Wang, G. L., & Chew, W. C.**(2006). Efficient Low-Frequency Inversion of 3D Buried Objects with Large Contrasts, *IEEE Transactions on Geoscience and Remote Sensing, 44*, 3-9.

[30] **Cui, T. J., Chew, W. C., Aydiner, A. A.,& Chen, S.**(2001). Inverse Scattering of Two-Dimensional Dielectric Objects Buried in a Lossy Earth Using the Distorted Born Iterative Method, *IEEE Transactions on Geoscience and Remote Sensing, 39*, 339-346.

[31] **Li, F., Liu, Q. H., & Song, L.**(2004). Three-Dimensional Reconstruction of Objects Buried in Layered Media Using Born and Distorted Born Iterative Methods, *IEEE Geoscience and Remote Sensing Letters,1*, 107-111.

[32] **Nehari, Z.**(1975). *Conformal Mapping.* New York, NY.: Dover Publications

[33] **Altuncu, Y., Yapar, A., & Akduman, I.**(2007). Numerical Computation of the Green's Function of a Layered Media with Rough Interface, *Microw. Opt. Technol. Letters,49*, 1204-1209.

[34] **Sommerfeld, A.**(1949). *Partial Differencial Equations in Physics.* New York, NY.: Academic Press.

[35] **Colton, D.,& Kress, R.**(1998). *Inverse Acoustic and Electromagnetic Scattering Theory.* Berlin : Springer.

[36] **Gao, G., Torres-Verdin, C., & Habashy, T. M.**(2005).Analytical Techniques to Evaluate the Integrals of 3D and 2D Spatial Dyadic Green's Functions, *Progress in Electromagnetics Research, PIER, 52*, 47-80.

[37] **Van Den Berg, P. M., & Kleinman, R. E.**(1997). A Contrast Source Inversion Method, *Inverse Problems, 13*, 1607- 1620.

[38] **Hackbusch, W.**(1994). *Iterative Solution of Large Sparse Systems of Equations.* New York, NY.: Springer.

[39] **Tijhuis, A. G.**(1989). Born-Type Reconstruction of Material Parameters of an Inhomogeneous Lossy Dielectric Slab from Reflected-Field Data, *Wave Motion,11*, 151-173.

[40]**Roger, A.**(1981). A Newton-Kantorovich Algorithm Applied to an Electromagnetic Inverse Problem, *IEEE Trans. Anten. Propagat., 29*, 232-238.

[41] **Tabbara, W., Duchene, B., Pichot, C., Lesselier, D., Chommeloux, L., & Joachimowicz, N.**(1988). Diffraction Tomography: Contribution to the Analysis of Applications in Microwaves and Ultrasonics, *Inverse Problems,4*, 305-331.

CIRRICULUM VITAE

Name Surname: Evrim Tetik

Place and Date of Birth: Çanakkale, March 13th, 1978

E-Mail: tetike@itu.edu.tr

B.Sc.: I.T.U. Electronics and Communication Engineering

M.Sc.: I.T.U. Satellite Communication and Remote Sensing

Professional Experience:

Istanbul Technical University, Faculty of Electrical and Electronics
Engineering   2005-2013
Research & Teaching Assistant

PUBLICATIONS BASED ON THESIS

▪ **Tetik E.**, Akduman I., 2015: 3D Imaging of Dielectric Objects Buried Under a Rough Surface by using CSI. *International Journal of Antennas and Propagation - ,.* (Accepted)

▪ Güren O.,**Tetik E.,** Ergene L, Akduman I., Çayören M, 2011: A 3D Microwave Surface Impedance Approach for the Detection of Breast Cancer − *ISMOT 2011*, Prague, June